NANO LETTERS

Letter

pubs.acs.org/NanoLett

Direct Observation of Metal–Insulator Transition in Single-Crystalline Germanium Telluride Nanowire Memory Devices Prior to Amorphization

Pavan Nukala,[†] Rahul Agarwal,[†] Xiaofeng Qian,[‡,§] Moon Hyung Jang,[†] Sajal Dhara,[†] Karthik Kumar,[†] A. T. Charlie Johnson,[†,∥] Ju Li,[‡,§] and Ritesh Agarwal*[,†]

[†]Department of Materials Science and Engineering, University of Pennsylvania, Philadelphia, Pennsylvania 19104, United States

[‡]Department of Nuclear Science and Engineering and [§]Department of Materials Science and Engineering, Massachusetts Institute of Technology, Cambridge, Massachusetts 02139, United States

[∥]Department of Physics and Astronomy, University of Pennsylvania, Philadelphia, Pennsylvania 19104, United States

Supporting Information

ABSTRACT: Structural defects and their dynamics play an important role in controlling the behavior of phase-change materials (PCM) used in low-power nonvolatile memory devices. However, not much is known about the influence of disorder on the electronic properties of crystalline PCM prior to a structural phase-change. Here, we show that the application of voltage pulses to single-crystalline GeTe nanowire memory devices introduces structural disorder in the form of dislocations and antiphase boundaries (APB). The dynamic evolution and pile-up of APBs increases disorder at a local region of the nanowire, which electronically transforms it from a metal to a dirty metal to an insulator, while still retaining single-crystalline long-range order. We also observe that close to this metal–insulator transition, precise control over the applied voltage is required to create an insulating state; otherwise the system ends up in a more disordered amorphous phase suggesting the role of electronic instabilities during the structural phase-change.

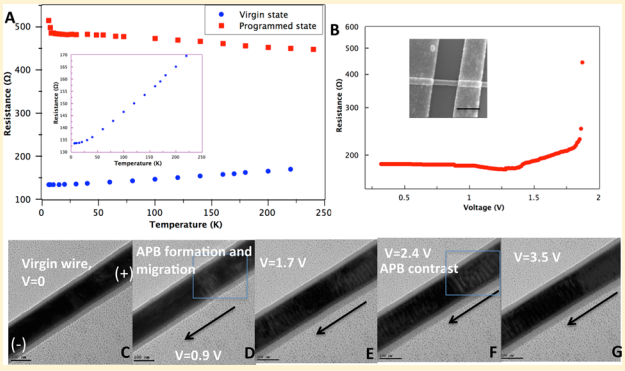

KEYWORDS: *GeTe, phase-change memory, antiphase boundary, weak localization, metal-insulator transition, in situ microscopy*

While traditionally crystal-to-amorphous phase transformation in phase-change materials (PCM) has been believed to involve the melt-quench mechanism,[1] it is now being realized[2−4] that such a transformation could also occur more subtly, through the evolution of a variety of defects. There have been considerable theoretical studies on the energetics of formation and motion of intrinsic point defects, which are unique to crystalline PCM, and their effect on the electronic properties of PCMs.[5−9] Recently, Seigreist et al.[10] demonstrated insulator-to-metal transition in $GeSb_2Te_4$ thin-films via annealing, suggesting the role of vacancy ordering in the evolution of material properties. However, none of these studies directly relate the evolution of disorder and its effect on the electronic properties in a functioning device under electrical pulsing. Observations of real time microstructural changes using transmission electron microscopy (TEM) by Nam et al.,[4] have shown the crucial role of extended defects such as dislocations, formed by vacancy condensation, during the amorphization of single-crystalline $Ge_2Sb_2Te_5$ nanowires.[4] However, these studies have not elucidated the effects of defect dynamics on the evolution of the electronic structure in the crystalline state of PCM, where long-range order is still maintained. It is possible that these point defects evolve into extended defects during memory switching, thereby significantly altering the electronic structure.[5] Here, by establishing structure–property correlation during the application of voltage pulses via temperature-dependent resistance measurements, and Fourier and real space in situ TEM characterization on single-crystalline GeTe phase-change memory devices, we show that GeTe transitions from a metal to a weakly localized metal and finally to an insulating (but single-crystalline) state, prior to amorphization, aided by disorder. Our results demonstrate the critical role of intrinsic point defects and extended defects on the electronic structure of GeTe and suggest that such electronic phase transition prior to amorphization could be intrinsically responsible for the rapid structural phase transformation in PCM.

We selected GeTe as a system of choice owing to its well-understood atomic structure and relatively simple binary chemical composition, which makes the interpretation of

Received: February 24, 2014
Published: March 14, 2014

   dx.doi.org/10.1021/nl5007036 | *Nano Lett.* 2014, 14, 2201−2209

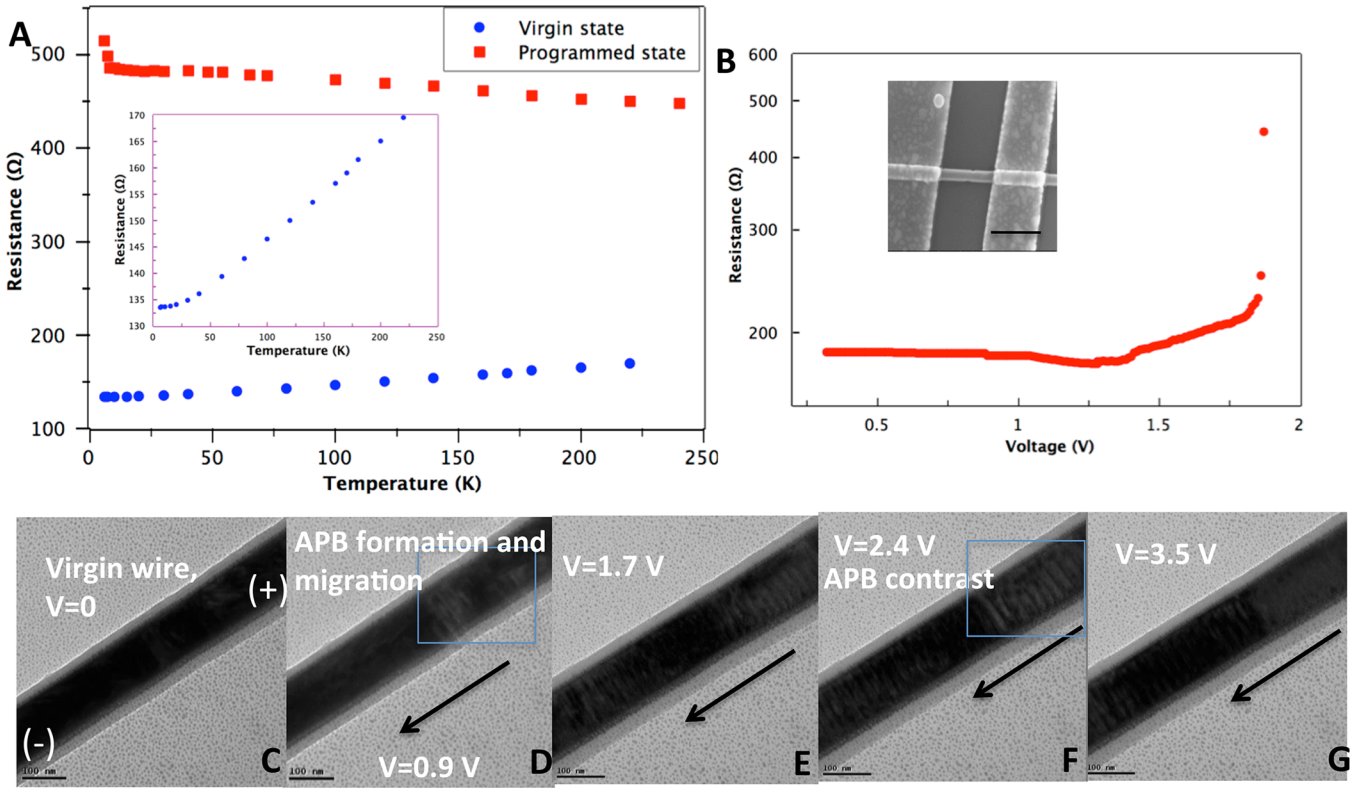

Figure 1. Electronic and structural changes in a GeTe nanowire phase change memory device upon programming prior to amorphization. (A) Plot of temperature versus resistance ($T-R$) of the nanowire in both virgin state (blue circles) and programmed state (red squares) from 5 to 240 K, clearly indicating a change in slope of the TCR upon programming. (Inset) zoomed in virgin state's $T-R$ plot clearly indicating positive TCR and saturating resistance as temperature approaches 0 K, or metallic behavior. (B) The programming curve for the device whose $T-R$ characteristics are shown in (A). (Inset) SEM micrograph of the device. Scale bar, 1 μm. (C) Virgin (unprogrammed) GeTe nanowire device capped with a 15 nm silicon oxide shell. In situ BFTEM was performed on this device during the initial stages of programming. The polarity of the electrodes are indicated. (D–G) Snapshots from the Supporting Information, Movie S1 (BFTEM movie during programming), shows APB evolution at different voltages. (D) The initial stages of formation of APBs at ~1 V. (E–G) Migration of APBs in the direction of hole-wind force, as indicated by the arrows. Scale bar in all the panels from C–G is 100 nm.

structure–property correspondence easier in comparison with other Ge–Sb–Te ternary alloys. GeTe exists in a stable rhombohedral structure (α = 88.35°, space group: $R3m$; ferroelectric phase) at room temperature and has 8–10% Ge vacancies ($\rho_v \approx 10^{19}/cm^3$)[5,11,12] as the most easily formed intrinsic defects at equilibrium.[6] The presence of such high concentration of Ge vacancies is responsible for p-type metallic conduction in crystalline GeTe;[5,6] that is, Fermi level (E_f) is 0.1–0.5 eV inside the valence band.[5,13] GeTe can also exist in a metastable cubic phase (paraelectric phase), which is also metallic due to the presence of a large number of Ge vacancies.[5,6] However, formation of other kinds of defects (such as Te antisites, which have a higher formation energy than Ge vacancies) especially during device operation can significantly affect the local electronic density of states[5] by creating localized electronic states and hence can play a pivotal role in electronic and structural transitions in the system.

Single-crystalline rhombohedral GeTe nanowires were grown along ⟨110⟩ direction via the vapor–liquid–solid[14] process (Supporting Information, Figure S1). To enable in situ TEM structural characterization, GeTe nanowire devices were fabricated on a special device platform.[4] Temperature-dependent resistance measurements were performed on GeTe devices fabricated on SiO_2/Si substrate (Supporting Information, Figure S2). All the devices were operated through the application of voltage pulses (a few tens of nanoseconds in duration) with a time lag of 2 s between every two pulses to ensure complete thermalization of the device. Steady-state resistances were measured one second after the application of every voltage pulse using low-bias direct current (dc) $I-V$ sweeps. These steady state resistance values as a function of the applied pulse amplitude are referred to as "programming curve", and the process of application of voltage pulses is referred to as programming.

The temperature-dependent resistance data (Figure 1A, blue curve) of a virgin (unprogrammed) GeTe nanowire device (Figure 1B, inset) displays a positive temperature coefficient of resistance (TCR), that is, the resistance decreases linearly with decreasing temperature until ~50 K and then approaches a saturation value (Figure 1A, inset) as the temperature approaches absolute zero. This is characteristic of metallic behavior, as is expected for crystalline GeTe[13] where the electron mean free path (l) is determined by electron–phonon scattering at higher temperatures (linear regime) and by defect scattering at lower temperatures (saturation regime). Data on more virgin state (unprogrammed) nanowire devices are shown in Supporting Information, Figure S3, which show a similar behavior. However, after programming the nanowire (amplitude range; 0.1–1.8 V, 50 ns pulses) (Figure 1B) to a state prior to amorphization, the TCR of the same device now becomes negative (Figure 1A, red squares), which demonstrates a change in the metallic nature of conduction. The

dx.doi.org/10.1021/nl5007036 | Nano Lett. 2014, 14, 2201–2209

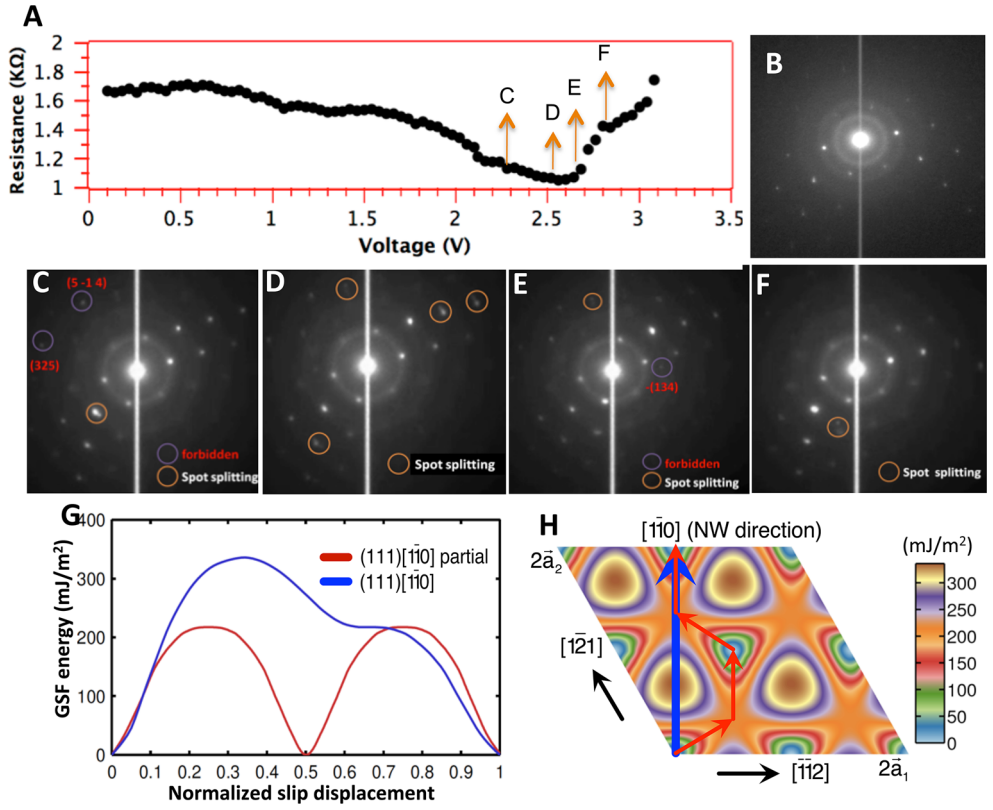

Figure 2. Fourier space imaging of a GeTe nanowire device during programming and GSF calculations for understanding the dislocation motion. (A) Programming curve for the device on which in situ Fourier space imaging has been performed while being programmed. (B) SAD of the virgin state of the device (see Supporting Information, Figure S1 for spot indexing). (C–F) SAD snapshots of a video (Supporting Information, Movie S3) recorded during programming. C–F are indicated on the programming curve (A). Indexed forbidden spots are shown in red. FCC nomenclature has been used to index spots. In this nomenclature, an allowed spot is a plane represented as (hkl), where h,k,l are all odd or even together (same parity). If they have a mixed parity, then that spot is a forbidden reflection. Split spots are circled in white and indexed. (G) GSF versus slip displacement of a dislocation in (111) $[1\bar{1}0]$ slip system (blue curve), and associated partials (red curves) in (111) plane. (H) A 2D GSF plot in the (111) plane with directions indicated in blue and red arrows.

nature of this electronic transformation in GeTe from its pure metallic state during programming will be discussed in detail later.

In order to correlate these electronic changes in GeTe to structural evolution, in situ real and Fourier space analyses (selected area diffraction (SAD)) were performed on TEM compatible devices during programming (Supporting Information, Figure S1C). In situ bright-field TEM (BFTEM) analysis was carried out on a 15 nm silicon oxide capped GeTe nanowire device[16] (programming curve with 50 ns voltage pulses is shown in Supporting Information, Figure S4), and the microstructural dynamics during programming were recorded in Supporting Information, Movie S1 (snapshots in Figure 1C–G), which reveals the formation of dislocations (see Supporting Information, Figure S5 for tilt analysis of dislocations) and antiphase boundaries (APBs) at ~0.9 V (Figure 1D), and their migration along the direction of the hole-wind force (Figures 1E–G). The application of a short voltage pulse that produces heat shocks in the nanowire creates Ge vacancy clusters, which beyond a certain size would prefer to condense in the {111} plane causing local collapse of two adjacent atomic planes and formation of edge dislocation loop (Supporting Information, Movie S2).[4,7] These vacancy loops (dislocations) can expand by absorbing other Ge vacancies and multiply like Frank loops.[4] The resulting decrease in the Ge vacancy (dopant) concentration in the system would lead to a reduction in the hole-carrier concentration. In order to verify this, electron energy loss spectroscopy (EELS) was performed during the programming, which indeed shows a shift in the bulk plasmon peak from 16.4 eV (virgin device) to 17.4 eV (programmed device) (Supporting Information, Figure S6). The shift in the bulk plasmon peak results from a decrease in hole concentration upon programming (see Supporting Information for relation between the frequency of the bulk plasmon and hole-carrier concentration[15]). As illustrated in Supporting Information, Movie S2, associated with the Ge vacancy loop formation is the creation of APBs, which in an atomistic picture is formation of a series of ordered Te antisites. Upon the application of short voltage pulses, these APBs migrate along the direction of the carrier-wind force (Supporting Information, Movie S1, Figure 1D–G).

In situ Fourier space analysis and generalized stacking fault (GSF) energy calculations using density functional theory (DFT) further reveals the dynamics of these dislocations upon programming. SAD patterns recorded (Supporting Information, Movie S3) from the device (selected area shown in Supporting Information, Figure S1C) during programming from its virgin state (Figure 2B and indexed in Supporting Information, Figure S1) show that some forbidden spots appear and disappear as a function of applied voltage pulses, while some spots elongate, split, and subsequently heal themselves (Figure 2C–F). All these changes happen in the spots

dx.doi.org/10.1021/nl5007036 | Nano Lett. 2014, 14, 2201–2209

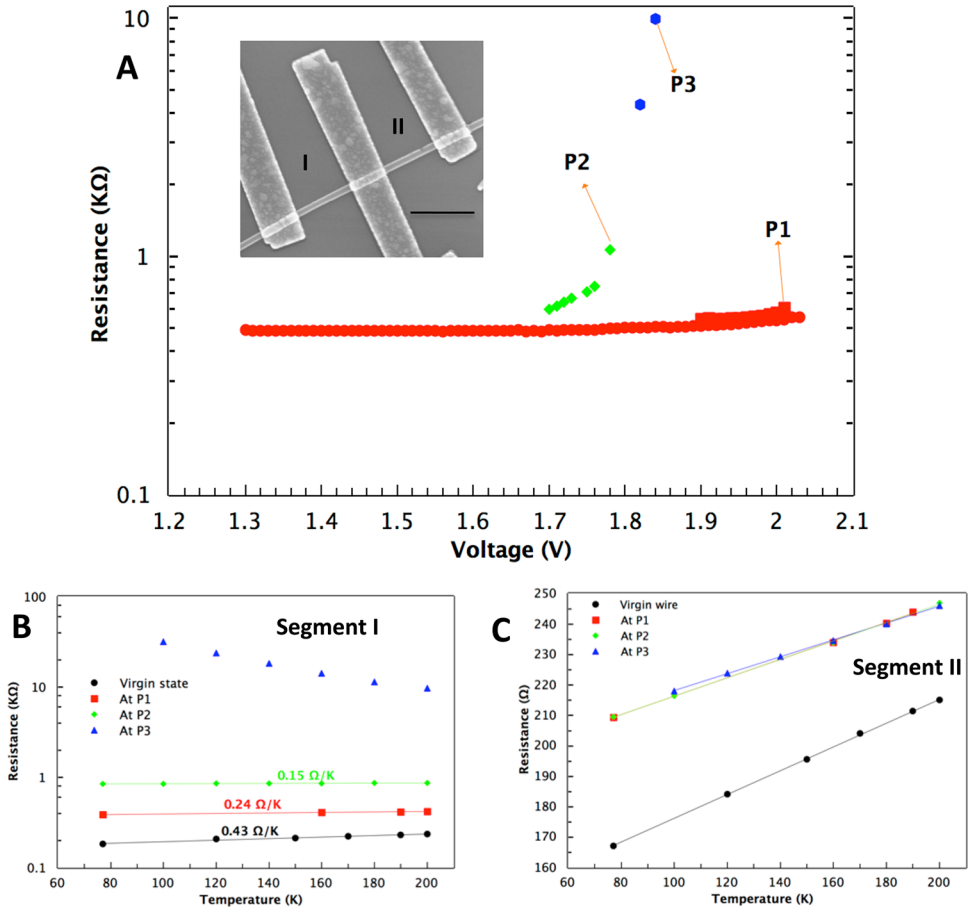

Figure 3. *T*−*R* curve of a three terminal GeTe nanowire device to show the electronic changes upon programming occur locally. (A) Programming curve of the device, which is carried out between the extreme electrodes. (Inset) SEM micrograph of the device, showing the two segments, I and II. Scale bar, 2 μm. *T*−*R* measurements were conducted on each individual segment at P1, P2, and P3 points. (B) *T*−*R* plots of segment I in its virgin state (black dots) after programming up to P1, P2, and P3 (red squares, green diamonds, and blue triangles, respectively). All significant changes in resistance of the total wire come from this segment. (C) *T*−*R* plots of segment II in its virgin state (black dots) and after programming up to P1, P2, and P3 (red squares, green diamonds, and blue triangles, respectively). After an initial increase in resistance by ∼50 Ω, the TCR and the resistances themselves remain unaffected by programming (see table in Supporting Information, Figure S10).

corresponding to higher order reflections indicating structural distortions at a length-scale less than the lattice parameter. Appearance of forbidden spots is a result of perturbation in long-range structural order caused by presence of dislocation cloud (as also shown by BFTEM, in real space), and their disappearance is as a result of migration of these dislocations during the initial stages of programming. Furthermore, the appearance of forbidden spots at only the higher orders of reflection in the SAD pattern of all the devices analyzed, indicates the existence of partial dislocations (disruption of lattice by less than a unit cell distance). Spot splitting in diffraction is a characteristic of 2D defects,[15] APBs in this case (and not microtwins, see Supporting Information for more discussion).

Generalized stacking fault (GSF) energies of {111} $\langle 1\bar{1}0\rangle$ family of slip systems calculated through DFT (see Supporting Information and Figures S7 and S8) show a maximum value of 340 mJ/m^2 for perfect (defect-free) GeTe (Figure 2G). It must be noted that the carrier-wind force is along the nanowire growth axis $\langle 110\rangle$ direction, and hence (111) $[1\bar{1}0]$ slip system has been considered as the most relevant slip system (see Supporting Information for GSF calculations for other competing slip systems and Supporting Information, Figure S8). A 2D plot of GSF in the (111) plane (Figure 2H) further shows that when vacancy loops dissociate as partials (also revealed from diffraction) and propagate in the (111) plane (red path in Figure 2H), dissociation reaction being $[1\bar{1}0] = 2/3[1\bar{1}0] + 1/3[10\bar{1}] + 1/3[0\bar{1}1]$, they encounter a lower energy barrier (217 mJ/m^2) and stable stacking faults. In addition, the presence of ∼8% Ge vacancies is expected to reduce the GSF further, which would enable facile movement of dislocations in the direction of carrier wind-force (see Supporting Information for more discussion on dislocation dynamics).

Although these experiments demonstrate that during programming Ge vacancies are being condensed to form Te antisites (due to dislocations), it is unlikely that this initial dislocation migration, which creates defects and subsequently heals the crystal, may cause any permanent structural change responsible for the observed change of TCR (Figure 1A). To understand at what stage during the programming does TCR change its sign, and if these changes happen locally or globally in the nanowire, we fabricated devices with multiple electrodes, where the programming was done between the outermost electrodes (Figure 3A and Supporting Information, Figure S10). Temperature-dependent resistance measurements of individual segments were obtained at representative points labeled P1, P2, and P3 in Figure 3A. After reaching P1, the TCR of the device was measured, and then the device was

dx.doi.org/10.1021/nl5007036 | *Nano Lett.* 2014, 14, 2201−2209

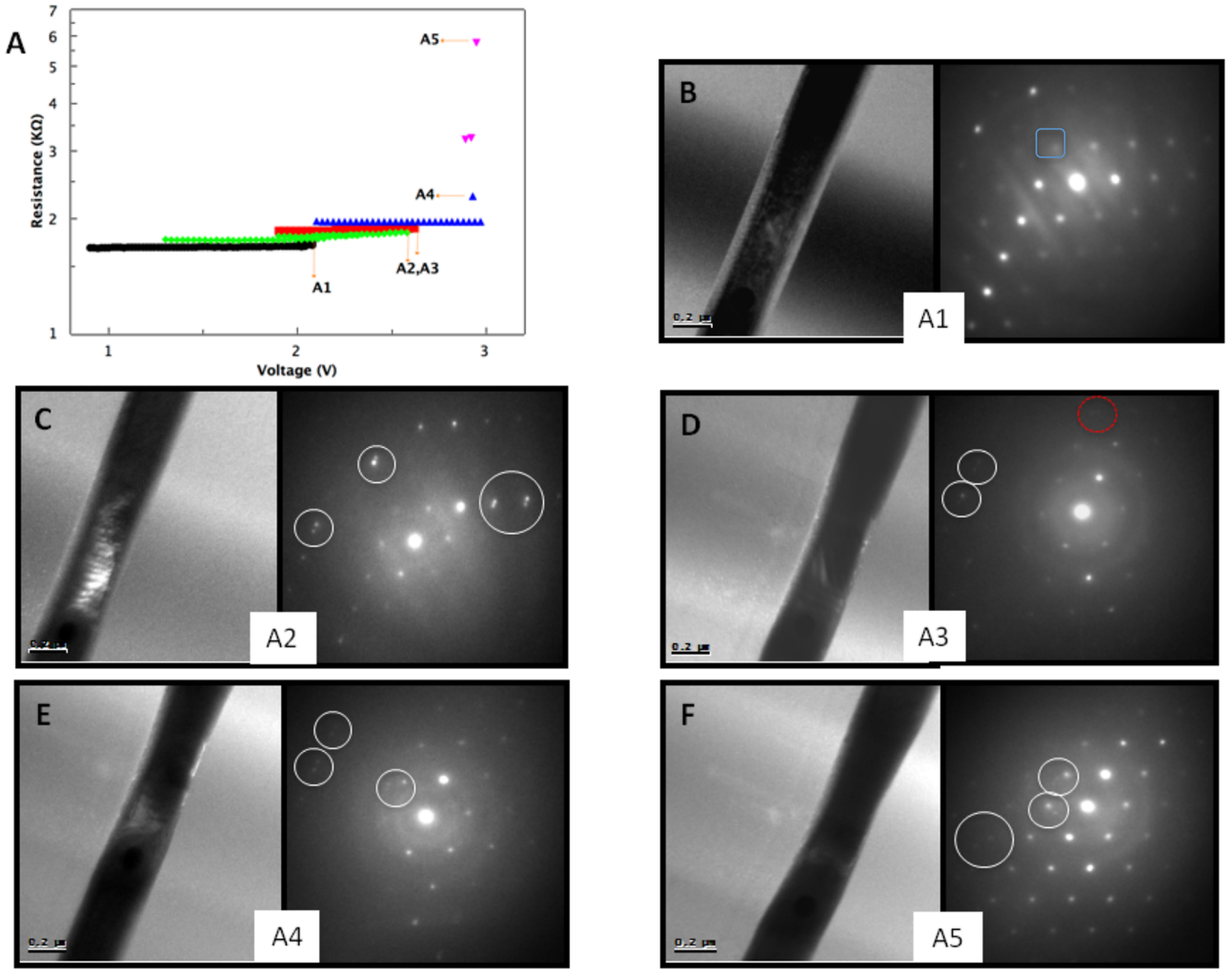

Figure 4. Structural changes in a GeTe nanowire device via in situ TEM measurements showing the formation and smearing of antiphase boundaries in a localized region. (A) Programming curve of the device. A1−A5 are the points in the curve after which DF images along with SAD were acquired. (B) At A1, which is similar to the virgin state. (C) At A2, where DF image shows a clear APB contrast. DF images were obtained from the diffraction spot bounded by blue rectangle. SAD shows spot splitting (circled in white) along the growth direction. (D) At A3, DF image shows contrast from two intersecting set of APBs from different {111}. SAD shows spots splitting along the growth direction (circled in white), and along another ⟨110⟩ direction (circled in red), indicating two different sets of APBs. (E) At A4, DF shows smearing of APB contrast while SAD shows extra spots and spot splitting. (F) At A5, SAD shows a clear splitting of the spot in the first order of reflections.

reprogrammed (between extreme electrodes) starting at ∼1.6 V, (this process was repeated after P2). As can be seen in Figure 3A, the increase in resistance of the entire wire becomes drastic from P1, which necessitated the pull back and careful control of the pulse amplitude in order to avoid amorphization of the device (Supporting Information, Figure S9). It was observed that almost all the increase in the resistance values observed in the programming curve came from segment I, and not II (Supporting Information, Figure S10). Similarly, temperature dependence of resistance of segment II (Figure 3C) at P1, P2, and P3 essentially remains the same, clearly demonstrating that programming did not affect this segment electronically. However, TCR of segment I (Figure 3B) reduced from 0.43 Ω/K in virgin state to 0.24 Ω/K upon programming up to P1 and to 0.15 Ω/K at P2. After P2, the resistance of segment I increased discontinuously by an order of magnitude (from 800 Ω to 9 KΩ) within a span of just two voltage pulses (∼1.8 V) to reach P3, which is achievable only through controlled voltage pulsing to avoid amorphization (see Supporting Information, Figure S9 for data on a device that was not programmed in a controlled way, and hence it amorphized). At P3, the resistance of segment I displays strong temperature dependence and decreases nonlinearly with temperature. (The exact conduction characteristics at P2 and P3 of segment 1 are discussed later.) Similar data are obtained from other devices (Supporting Information, Figure S11), which demonstrate that electronic changes occur locally in the nanowire, and this is intimately linked to the dislocations getting jammed above a certain voltage threshold during the programming.[4]

To correlate the observed electrical characteristics to the local structural changes at a later stage of programming, in situ TEM analyses were performed on GeTe devices (capped with SiO_x to improve device stability[4,16]). At different points on the programming curve (Figure 4A, A1−A5) SAD patterns along with displaced aperture dark-field (DF) images[17] were acquired. At point A1 (Figure 4B), SAD and DF image do not show any significant changes from the virgin state. However, at point A2 (Figure 4C), DF image shows a clear APB contrast, while SAD shows the corresponding spot-splitting along the growth

dx.doi.org/10.1021/nl5007036 | Nano Lett. 2014, 14, 2201−2209

direction,[17] demonstrating that APBs have created a translational disorder along the growth direction (one of the ⟨110⟩ directions). It is important to note that any changes in diffraction patterns (spot splitting) at A2 are observed only beyond the spots corresponding to second order of reflections. APBs, owing to their fault energy, reduce the mobility of dislocations that pass through them, and once enough APBs accumulate in a local region, dislocation migration along the carrier wind force direction (growth direction) becomes energetically unfavorable. Instead, the system then activates dislocation slip in other {111} slip-planes along the nongrowth direction (other ⟨110⟩ directions), generating more APBs that cause a translational disorder in that direction; this is observed at A3 (Figure 4D) where DF image shows the intersection of two sets of APBs in different {111} family of planes. Diffraction reinforces this observation with distinct spot-splittings in two different directions (circled in white and red respectively in Figure 4D) corresponding to two sets of APBs, one along the growth direction and other in another ⟨110⟩ direction. All these changes still happen beyond the second order of reflections. At A4, the programming curve shows the onset of a drastic increase in device resistance, necessitating controlled programming to avoid amorphization. DF imaging at A4 (Figure 4E) shows smearing of the APB contrast, owing to several overlapping sets of APBs, or arrest of dislocation mobility in most of the slip planes. This corresponds to the dislocation jamming process[4] and creates a huge density of Te antisites (many intersecting APBs), which are no longer ordered. Smearing of APB contrast is an effect of loss of coherence of scattered electrons owing to heavy disorder.[17] At this stage, the diffraction pattern shows extra spots between first and second order of reflections, owing to a heavy disruption of order in the observed zone. Further programming discontinuously increased the resistance by 3 KΩ in a span of 3 pulses to reach A5 (Figure 4A). Corresponding SAD data now shows spot splitting in the first order of reflections itself (Figure 4F). Spot splitting progressively moving toward the first order of reflections only in a local region with programming, clearly suggests increasing disorder (Te antisites) in the observed [111] zone (see Supporting Information for a detailed discussion) being responsible for the changes in electrical properties (which also occur locally).

To characterize the electronic states of GeTe as it undergoes programming (prior to amorphization), temperature-dependent resistance data acquired from segment I (2 μm long) of the device shown in Figure 3A at P2 and P3 were further analyzed. The resistance of the local disordered region contributing to the change in TCR of the programmed device at each temperature was estimated by subtracting the metallic phase resistance (a very small component) from the total resistance (see Supporting Information for details on the estimation). At P2 (corrected resistance of the local region is shown in Figure 5A), three distinct regimes can be identified: at temperatures >50 K, resistance decreases linearly with increasing temperature, saturates in the 10−50 K region, and shows a rapid increase for temperatures <10 K. Similar behavior is also observed in a short (1 μm) programmed device shown in Figure 1B (see Supporting Information, Figure S12) even without correcting for the resistance of the disordered region, owing to the relatively large contribution of resistance from the local disordered region to the total resistance (see Supporting Information). The three regimes, linear, saturation and rapid increase marked in Figure 5A are consistent with the characteristics of a "dirty metal",[18−22] which refers to a disordered metal, displaying the effects of incipient (weak) localization.[19−22] Weak localization is a quantum-mechanical effect, where the electrons form standing waves by constructively interfering between two time reversed trajectories after undergoing multiple scattering by defects, the amplitude of which increases with defect density,[19,21] thereby giving rise to residual resistivity, ρ_0 (saturation regime). The saturation regime (Figure 5A) at low temperatures (10−50 K) is observed because temperature does not have much effect on quantum interference as long as the carrier mean free path (l_P) due to phonon scattering is greater than the phase correlation length (ξ).[20] Increasing the temperature reduces l_P, and at higher temperatures when $l_P < \xi$ carrier scattering by phonons reduces the effect of weak localization[19−22] resulting in decreased resistance, which explains the linear regime in Figure 5A, and the negative TCR associated with it. However, below 7 K (Figure 5A) there appears to be a divergence in the resistance but given the small magnitude of resistance increase, we believe it may not be an actual divergence as expected from an insulating state.[23] Anomalies in the behavior of dirty metals at very low temperatures can be explained by considering possible electron−electron correlation effects,[19,24] which have also been recently demonstrated in PCM.[25] Therefore, GeTe until state P2 is in the dirty metal limit, which is very close to the metal−insulator transition (MIT), but is still metallic.

What remains to be seen is if further addition of disorder to GeTe in a dirty metal state can lead to an insulating state, that is, disorder-induced electronic localization[23,26] of states close to the mobility edge, E_m,[23] that is, Anderson's localization. A material is an insulator with thermally activated conduction if E_f is located in these localized states and a metal if the E_f is in the extended states (Figure 5C). There will be a metal−insulator transition (MIT) if the sign of $E_f - E_m$ changes.[23] However, the sign of $E_f - E_m$ for GeTe in the dirty metal limit (P2 in Figure 3A) remains negative (E_f inside the valence band) and it is still metallic.[18]

Following P2 (Figure 3A), a couple of pulses at ∼1.8 V increased the resistance of the device by an order of magnitude (800Ω to 9 KΩ) to state P3, which showed a stronger (as compared to P2) and nonlinear dependence of resistance on temperature (Figure 3B). Figure 5B shows the temperature versus corrected resistance characteristics of the state P3 with a conduction mechanism that fits the variable range hopping (VRH[27]) model ($\log \sigma \sim T^{-0.25}$, where σ is the material conductivity) from 100 to 340 K. VRH describes conduction of electrons via quantum-mechanical tunneling between the localized states, which means that E_f has effectively crossed E_m and moved into the localized states, corresponding to a metal-to-insulator transition (MIT). It is worth mentioning here that the insulating phase is electronically and structurally different from the amorphous phase of GeTe. Amorphous GeTe also displays VRH conduction at low temperatures (<200 K)[28] but changes to Poole−Frenkel mechanism ($\log \sigma \sim 1/T$)[28,29] above 200 K with activation energy for conduction being equal to half the band gap energy. This is indicative of E_f being pinned in the midgap, a typical characteristic of chalcogenide glasses.[23] The insulating phase demonstrated here shows VRH conduction up to higher temperatures (340 K) and no Arrhenius conduction behavior, indicating that E_f is still close to the valence band-edge (though above the mobility edge). Structurally, the insulating phase is a single-crystalline phase with long-range order as evidenced by diffraction and not

dx.doi.org/10.1021/nl5007036 | Nano Lett. 2014, 14, 2201−2209

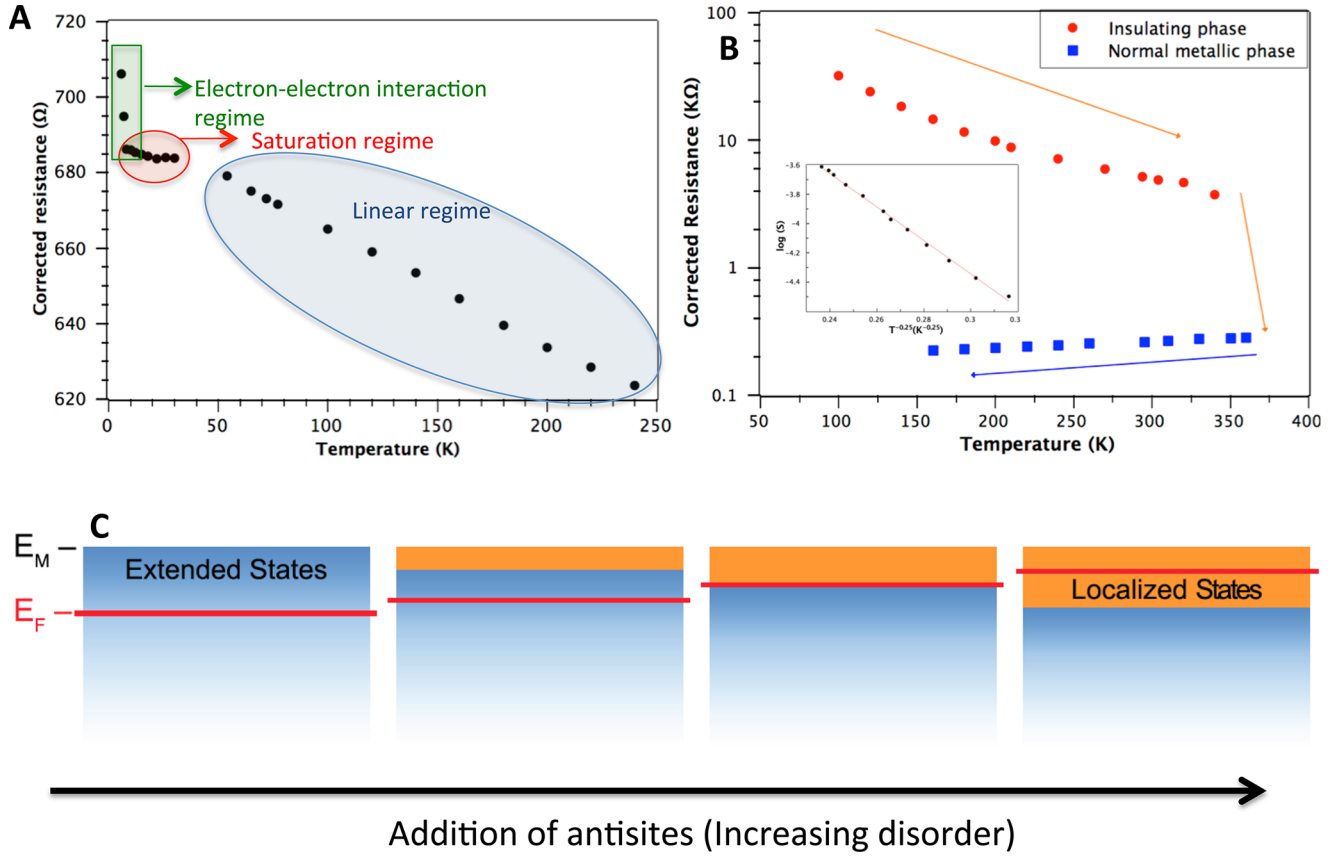

Figure 5. Electronic changes in GeTe from a metal to a dirty metal to finally a localized, insulating state upon controlled programming. (A) Temperature versus corrected resistance of the disordered region (at P2 from segment I, Figure 2A) showing characteristics of a dirty metal. (B) Temperature versus corrected resistance corresponding to the disordered region (at P3 from segment I, Figure 2A. The TCR (red circles and inset) shows the formation of an insulating phase due to the variable range hopping (VRH) mechanism of conduction, indicating a metal−insulator transition (MIT). The orange arrow indicates heating cycle. The insulating phase transforms to a metallic phase upon annealing above 340 K. The blue arrow indicates cooling cycle. (C) Schematic of the disorder induced metal to dirty metal to insulator transition. Addition of APBs adds localized states (orange) close to the band edge and also moves E_f closer to E_m. Weak localization effects take place when E_f approaches E_m but is still on the extended side (blue region) (dirty metal state represented in (A)). When E_f goes past E_m into the localized states, MIT takes place and VRH conduction mechanism is observed (state represented in (B)).

amorphous (A5 in Figure 4A corresponds to P3 in Figure 3A as explained below). Upon annealing, this insulating (Anderson localized) phase is not stable beyond 70 °C (Figure 5B, also see similar data from another device in Supporting Information, Figure S13B), while the amorphous phase in GeTe is stable in a much larger temperature window (~230 °C).[13,30] It is important to mention here that upon programming, weak localization behavior was observed on all the 25 devices we tested (for representative data on more devices showing weak localization see Supporting Information, Figures S11B and S14), whereas through careful programming we were successfully able to convert 70% of the devices into insulating phase (as indicated by the discontinuous resistance change in the programming curve) without amorphizing them (unlike the device data in Supporting Information, Figure S9). We could measure the VRH conduction characteristics on six of these insulating state devices (for representative data on insulating phase, and metal−dirty metal−insulator transition on more devices see Supporting Information, Figures S13(B) and S14 respectively), while the others spontaneously transformed to the metallic state during the temperature-dependent measurements.

The model described in Figure 5C, explains the observations of conduction mechanisms at different regimes of disorder, making one-to-one correspondence between structural changes and electronic changes. Virgin state in GeTe shows p-type metallicity, with $E_f - E_m < 0$. Upon application of voltage pulses, dislocations and APBs formed due to vacancy condensation migrate along the carrier wind force direction and eventually jam at a particular region in the nanowire. As a result, the disorder in GeTe keeps piling up at this local region in the form of Te antisites. Antisites introduce localized electronic states near the band (mobility) edge and moves E_f toward these states.[5] Initially antisites are ordered as APBs (A2 and A3 in Figure 4, P1 in Figure 3A,B), and this corresponds to a regime on the programming curve where resistance gradually increases with voltage (see Supporting Information, Figure S13A). With controlled programming, Te antisites become disordered as different sets of APBs intersect (P2 in Figure 3, A4 in Figure , and see Supporting Information), and this corresponds to the region in the programming curve that shows a rapid increase in resistance with voltage. Electronically, this is a dirty metal where the single-crystalline metallic nanowire shows effects of weak localization; nevertheless, is still metallic ($E_f - E_m$ remains negative). GeTe keeps getting "dirtier" with the addition of more disorder in a controlled fashion until it approaches the Anderson's limit. Further controlled programming takes the system to an insulating phase (MIT)

dx.doi.org/10.1021/nl5007036 | Nano Lett. 2014, 14, 2201−2209

characterized in the programming curve by a discontinuous increase in resistance by an order of magnitude (P3 in Figure 3A, A5 in Figure 4, also see Supporting Information, Figure S13(A)), with E_f now in the energy region of localized states ($E_f - E_m > 0$) and this phase exhibits VRH conduction, a signature of conduction in localized states. Structurally, this phase is still single-crystalline but perturbed by heavy local disorder.

This work for the first time demonstrates via structure–property correspondence that electronically GeTe can be controllably transformed from a metal to a dirty metal to an insulating state by progressive addition of disorder and not by chemical alloying. Furthermore GeTe is known to be a metal in all its known crystalline phases,[13] but our work shows that it can be transformed into an insulator while still being a single-crystal, thus discovering a new electronic phase in crystalline GeTe. MIT in GeTe occurs just prior to amorphization, and if care is not taken during programming near this transition the system ends up in an amorphous phase, suggesting the role of disorder and electronic instabilities during the amorphization process in PCM. Finally, our work bridges the gap between mesoscopic understanding of structural evolution, that is, evolution of extended defects, and atomistic understanding of structure–property correlation[5,7] in PCMs. The new insights it provides into the crystal-to-amorphous transformation can lead toward designing low-power strategies of switching in these fascinating materials. It is anticipated that similar structure–property correspondence studies along with advanced microscopy tools[31] can further illuminate on the atomistic processes responsible for field-induced phase transformations that can lead to deeper understanding of the efficient and ultrafast switching process in PCMs.

METHODS

Preparation of GeTe Nanowires. GeTe nanowires were synthesized using the metal catalyst mediated vapor–liquid–solid (VLS) process as described in ref 13. The as-grown nanowires were characterized by scanning electron microscopy (SEM, FEI DB strata 235 FIB), X-ray diffraction (XRD, Rigaku), and transmission electron microscopy (TEM, 200 kV JEOL 2010F, JEOL 2100) equipped with EDS (Energy Dispersive Spectroscopy). See Supporting Information, Figure S1.

Device Fabrication for TCR Measurements. Nanowires were dry transferred onto an insulating thermal oxide coated silicon substrate with predefined markers. Contacts to the nanowire were defined by electron-beam lithography (Ellionix, ELS-7500). Metallization was done by evaporating Ti–Au (10–120 nm). A thin protective oxide of SiOx (15 nm) was deposited using atomic layer deposition to cap the nanowires. These devices were tested using Lakeshore TTPX cryogenic probe station. Electrical measurements were performed with Keithley 2602 (I–V analyzer/Source meter), Keithley 2700 (Data acquisition, DAQ), and Keithley 3401 (pulse-generator). See Supporting Information, Figure S2.

Device Fabrication for in Situ TEM Observation. GeTe nanowire devices compatible with in situ TEM holder were fabricated by the procedure outlined in ref 4 (Supporting Information, Figure S2). Additionally a 15 nm protective SiO_x was deposited on the top of these devices using ALD just like in the case of the TCR devices. This removes any unwanted heating effects and improves device stability.[14] In situ TEM electrical testing was done using a home-built in situ TEM holder (described in ref 4) as an interface between the TEM and electrical measurement system (Keithley 2602 (I–V analyzer/Source meter), Keithley 2700 (Data acquisition, DAQ), and Keithley 3401 (pulse-generator)).

First-Principles Density Functional Theory Calculations. We performed the ab initio total energy calculations based on first-principles DFT using the Vienna Ab-initio Simulation Package (VASP) with the projector augmented wave (PAW) method[32] and a plane-wave basis with the kinetic energy cutoff of 227.5 eV.[33] Exchange-correlation functional in the Perdew–Berke–Ernzerhof (PBE)[34] form within the generalized gradient approximation (GGA)[35] was used in all DFT calculations. The low-temperature rhombohedral structure of GeTe crystal was fully relaxed by using Γ-centered 8 × 8 × 8 Monkhorst–Pack k-point sampling and a convergence criteria of 5×10^{-7} eV/atom and the maximum residual force less than 0.01 eV/ Å. Using the relaxed ground-state crystal structure, we set up three slab models (shown in Supporting Information, Figure S8) for the generalized-stacking-fault (GSF) energy calculations on three different slip planes, that is, (111), $(\bar{1}\bar{1}2)$, and (001). We adopted the Γ-centered 5 × 5 × 1, 3 × 3 × 1, and 4 × 4 × 1 Monkhorst–Pack k-point sampling schemes for the slips on three different planes (111), $(\bar{1}\bar{1}2)$, and (001), respectively. The total energy of each relaxed structure was calculated again with the more accurate tetrahedron zone summation with the Blöchl correction. The convergence criteria of 1×10^{-5} eV was used for both ionic and electronic relaxations. For the slip on (111) basal plane, we slid the top half of the supercell along both crystalline x- and y-direction on a 10 × 10 grid and calculated the corresponding two-dimensional GSF energy surface from which we obtained the GSF energy curves for both the direct and partial dislocation paths, that is, (111) $[1\bar{1}0]$ and $[1\bar{1}0] = 2/3[1\bar{1}0] + 1/3[10\bar{1}] + 1/3[0\bar{1}1]$. For the slip on (001) and $(\bar{1}\bar{1}2)$ planes, we slide the top half of the corresponding supercell along its closed packed direction ((001) [100] and $(\bar{1}\bar{1}2)$ $[1\bar{1}0]$) and obtained the GSF energy curve (shown in Supporting Information, Figure S8).

ASSOCIATED CONTENT

Supporting Information

Figures S1 to S14; Movies S1 to S3. This material is available free of charge via the Internet at http://pubs.acs.org.

AUTHOR INFORMATION

Corresponding Author

*E-mail: riteshag@seas.upenn.edu.

Author Contributions

P.N. and R.A. conceived and designed the experiments. P.N., R.A., and K.K. optimized the growth conditions, synthesized the nanowires, and performed structural and chemical characterization on them. P.N., R.A., M.H.J., and S.D. designed and modified the electrical setup used for both the in situ TEM experiments as well as TCR measurements. The in situ TEM holder was home-built in the lab of A.T.C.J. P.N. performed fabrication, TCR measurements, and in situ TEM experiments. X.Q. and J.L. performed ab initio calculations. P.N., R.A., X.Q., R.A., and J.L. interpreted and analyzed the data. P.N. and R.A. cowrote the manuscript. K.K made the illustrative Movie S2.

Notes

The authors declare no competing financial interest.

dx.doi.org/10.1021/nl5007036 | Nano Lett. 2014, 14, 2201–2209

■ ACKNOWLEDGMENTS

This work was supported by NSF (DMR-1002164 and 1210503), Penn-MRSEC (DMR05-20020), and Materials Structures and Devices Center at MIT. X.Q. and J.L. acknowledge the support by NSF DMR-1008104 and DMR-1120901. A.T.C.J. acknowledges the support of the Nano/Bio Interface Center through the National Science Foundation NSEC DMR08-32802. Electron microscopy experiments were performed at the Penn Regional Nanotechnology Facility at the University of Pennsylvania.

■ REFERENCES

(1) Raoux, S. *Annu. Rev. Mat. Res.* **2009**, *39*, 25.
(2) Kolobov, A. V.; Fons, P.; Frenkel, A.; Ankudinov, A. L.; Tominaga, J.; Uruga, T. *Nat. Mater.* **2004**, *3*, 703.
(3) Kolobov, A. V.; Krbal, M.; Fons, P.; Tominaga, J.; Uruga, T. *Nature Chem.* **2011**, *3*, 311.
(4) Nam, S.-W.; Chung, H.-S.; Lo, Y. C.; Qi, L.; Li, J.; Lu, Y.; Johnson, A. T. C.; Jung, Y.; Nukala, P.; Agarwal, R. *Science* **2012**, *336*, 1561.
(5) Edwards, A. H.; Pineda, A. C.; Schultz, P. A.; Martin, M. G.; Thompson, A. P.; Hjalmarson, H. P.; Umrigar, C. *Phys. Rev. B* **2006**, *73*, 045210.
(6) Edwards, A. H.; Pineda, A. C.; Schultz, P. A.; Martin, M. G.; Thompson, A. P.; Hjalmarson, H. P. *J. Phys: Condens. Matter.* **2005**, *17*, L329.
(7) Deringer, M. L. V.L; Stoffel, R. P.; Dronskowski, R. *Chem. Mater.* **2013**, *25*, 2220.
(8) Zhang, W.; Thiess, A.; Zalden, P.; Zeller, R.; Dederichs, P. H.; Raty, J.-Y.; Wuttig, M.; Blügel, S.; Mazzarello, R. *Nat. Mater.* **2012**, *11*, 952.
(9) Wuttig, M.; Lüsebrink, D.; Wamwangi, D.; Wenic, W.; Gillessn, M.; Dronskowski, R. *Nat. Mater.* **2007**, *6*, 122.
(10) Seigresit, T.; Jost, P.; Volker, H.; Woda, M.; Merkelbach, P.; Schlockermann, C.; Wuttig, M. *Nat. Mater.* **2011**, *10*, 202.
(11) Chattopadhyay, T.; Boucherle, J. X.; von Schnering, H. G. *J. Phys. C: Solid State Phys.* **1987**, *20*, 1431.
(12) Matsunaga, T.; Kojima, R.; Yamada, N.; Kifune, K.; Kubota, Y.; Tabata, Y.; Takata, M. *Inorg. Chem.* **2006**, *45*, 2235.
(13) Bahl, S. K.; Chopra, K. L. *J. Appl. Phys.* **1970**, *41*, 2196.
(14) Jennings, A. T.; Jung, Y.; Engel, J.; Agarwal, R. *J. Phys. Chem.* **2009**, *113*, 6898.
(15) Raether, H. *Excitation of Plasmons and Interband Transitions by Electrons*; Springer tracts in modern physics; Springer: New York, 1980; Vol. *88*.
(16) Meister, S.; Schoen, D. T.; Topinka, M. A.; Minor, A. M.; Cui, Y. *Nano Lett.* **2008**, *8*, 4562.
(17) Carter, C. B.; Williams, D. B. *Transmission electron microscopy: a textbook for materials science*; Springer: New York, 1996.
(18) Mooij, J. H. *Phys. Status Solidi* **1973**, *17*, 521.
(19) Lee, P. A.; Ramakrishnan, T. *Rev. Mod. Phys.* **1985**, *57*, 287.
(20) Imry, Y. *Phys. Rev. Lett.* **1980**, *44*, 469.
(21) Bergmann, G. *Phys. Rep.* **1984**, *107*, 1−58.
(22) Park, M.-A.; Savran, K.; Kim, Y.-J. *Phys. Status Solidi B* **2003**, *237*, 500.
(23) Mott, N. F.; Davis, E. A. *Electronic Processes in Non-Crystalline Materials*; Oxford University Press: Clarendon, 1979; Vol. *2*.
(24) Sacharoff, A. C. *Phys. Rev. B* **1982**, *26*, 5976.
(25) Breznay, N. P.; Volker, H.; Palevski, A.; Mazzarello, R.; Kapitulnik, A.; Wuttig, M. *Phys. Rev. B* **2012**, *86*, 205302.
(26) Anderson, P. W. *Phys. Rev.* **1958**, *109*, 1492.
(27) Zallen, R. *The Physics of Amorphous Solids*; John Wiley and Sons: New York, 1983.
(28) Longeaud, C.; Luckas, J.; Wuttig, M. *J. Phys: Conf. Ser.* **2012**, *398*, 012007.
(29) Nardone, M.; Simon, M.; Karpov, I. V.; Karpov, V. G. *J. Appl. Phys.* **2012**, *112*, 071101.
(30) Caldwell, M. A.; Raoux, S.; Wang, R. Y.; Wong, H.-S. P.; Milliron, D. J. *J. Mater. Chem* **2010**, *20*, 1285.
(31) Chen, C.-C.; Zhu, C.; White, E. R.; Chiu, C.-Y.; Scott, M. C.; Regan, B. C.; Marks, L. D.; Yu, H.; Miao, J. *Nature* **2013**, *496*, 74.
(32) Blöchl, P. E. *Phys. Rev. B* **1994**, *50*, 17953.
(33) Kresse, G.; Furthmuller, J. *Comput. Mater. Sci.* **1996**, *6*, 15.
(34) Perdew, J. P.; Burke, K.; Ernzerhof, M. *Phys. Rev. Lett.* **1996**, *77*, 3865.
(35) Langreth, D. C.; Mehl, M. J. *Phys. Rev. B* **1983**, *28*, 1809.

Supplementary Information for

Direct Observation of Metal-Insulator Transition in Single-Crystalline Germanium Telluride Nanowire Memory Devices Prior to Amorphization

Pavan Nukala, Rahul Agarwal, Xiaofeng Qian, Moon Hyung Jang, Sajal Dhara, Karthik Kumar, A.T. Charlie Johnson, Ju Li, and Ritesh Agarwal*

*To whom correspondence should be addressed. E-mail: riteshag@seas.upenn.edu

This file includes:

Supplementary Discussion
Figures S1-S14
Captions for Movies S1 to S3

Other Supplementary Information for this manuscript includes the following:

Movies S1 to S3

Characterization of rhombohedral structure of GeTe

The x-ray diffraction (XRD) results in figure S1 shows a clear splitting of the (111) (as (111) and $(11\bar{1})$) and (022) peaks. This is a clear indication of rhombohedral distortion (*R3m*). The virgin wire's diffraction pattern only contains allowed spots indicating relatively defect free single-crystalline phase to as a starting point (see figure S1).

Evidence of dislocations and APBs in GeTe upon programming

Figures 1C-G from the manuscript (snapshots from movie S1) and figure S5 show dislocation and APB contrast upon programming GeTe single-crystalline nanowires (programming curve for the device in movie S1 is shown in figure S4). Tilt analysis shown in figure S5 provides further proof (contrast smearing) of the presence of dislocations upon the application of short voltage pulses in these devices.

Peierls' distortion

Rhombohedral distortion in GeTe is a consequence of Peierls' distortion[5]. Geometrically rhombohedral distortion can accommodate Peierls' distortion more efficiently than a cubic symmetry. This is also reflected in our DFT calculations (see figure S8). When low temperature rhombohedral structure is relaxed, longer and shorter bonds between Ge and Te result, which is the manifestation of Peierls distortion. When viewed perpendicular to the basal plane (111) presence of long and short bonds is not apparent (as done in our TEM analysis; see figure S7 for various views of GeTe structure, and compare it with GST[4]).

Plasmonic spectroscopy: carrier counting

Bulk Plasmon peak positions were measured by performing electron energy loss spectroscopy (EELS) on GeTe nanowires both in the virgin state as well as in an early programming state (figure S6). The bulk plasmon peak position is directly related to the bound electron density in the system ($\omega_p^2 \sim N_{bound}$)[15]. Increase in the plasmonic frequency hence results from an increase in the bound electron density, or in other words decrease in hole concentration. Structural Ge vacancies in GeTe are responsible for p-type metallicity or a large hole concentration[5]. Decrease in the hole-concentration is directly related to the decrease in Ge vacancy (hole dopant) concentration.

GSF calculations on different slip systems

Figure S8 shows that dislocation dynamics in the (001)[100] slip system is also easy owing to comparable maximum GSF of partials in the $(111)[1\bar{1}0]$ slip system. However, since the hole-wind force is in the growth direction, say $[1\bar{1}0]$, $(111)[1\bar{1}0]$ is activated first. Then as revealed by the SAD patterns in figures 4C and 4D, other $\{111\}<1\bar{1}0>$ slip systems are activated. Following this, if amorphization does not yet take place, it is possible that other high-energy slip systems (shown in figure S8) are activated.

Dislocation dynamics in GeTe

We have shown indirectly through plasmonic spectroscopy that during electrical pulsing, Ge vacancies condense to form vacancy loops. These loops are formed in the {111} planes since they contain atoms of only one kind. Formation of these loops result in the formation of APBs in the {111} planes. Vacancy loops expand by absorbing other Ge vacancies[4] and multiply like Frank loops. Since the hole-wind force is along the growth direction, these loops effectively glide in the growth direction (movie S1). Movie S2 (also see figure S8E) shows the creation of such a vacancy loop in the $(\bar{1}11)$ plane, containing dislocation segments whose slip systems are $(111)[1\bar{1}0]$ and $(11\bar{1})$ $[1\bar{1}0]$ respectively, where $[1\bar{1}0]$ is the direction of hole-wind force. GSF calculations (figure 2G,H, figure S8) show that crystal shear can easily take place in the {111} plane containing longer GeTe bonds (figure S7B), through the dissociation of these dislocation segments into partials. The glide of vacancy loops along the direction of hole-wind force (growth direction) by dissociating into partials also means that the APBs propagate along the growth direction by splitting up as newer faults and recombining. Hence during the initial stages of dislocation motion APBs are formed in a particular region, and propagate away from that region, recovering the original crystallinity in that region (spots split and heal in SAD pattern in movie S3). When the mobility of the dislocations reduces at a local region of inhomogeneity, APBs accumulate in that local region. This further reduces the dislocation mobility, along the growth direction. Upon further supply of energy in the form of voltage pulses, the system prefers to activate slip systems, which are not along the growth direction (figure 4C-E). APB accumulation then happens in these new slip planes. When APBs in more than three sets of slip planes (there are four {111} family of planes) intersect, they form disordered Te antisites (which corresponds to a discontinuous increase in resistance in figure 3A, 4A).

Comment on the effect of vacancies on GSF

Figure S7 (C) shows the layered structure of $Ge_2Sb_2Te_5$. Every unit cell begins with a Te and ends in a Te. This means there must be Te-Te bond between two unit cells, and this bonding

is van der Waals in nature [4]. Some workers have interpreted these two Te layers as being separated by an ordered layer of Ge vacancies[36]. The GSF was reported to be ~10 $\frac{mJ}{m^2}$ in *ref.4* (comparable to graphene[4]), for basal slip along these layers. Figure S7 (B), on the other hand, shows the layered structure of GeTe. In GeTe, however, there are vacancies on Ge sites [5,6] present in a random fashion. The presence of vacancy eases the flow of dislocation at that atomic position, as the glide of dislocation through these vacancy positions does not need to break any chemical bonds (as in the case of GST there is almost no resistance for dislocation motion along the ordered vacancy plane). Hence, the presence of 8% vacancies on Ge sites, can to a first order of approximation be seen to be reducing the GSF linearly by 8%. Our GSF calculations (figures 2G,H, figure S8) did not take into account the presence of structural Ge vacancies. So, it is reasonable to estimate the 'real' GSFs to a good degree of approximation by reducing the calculated GSFs (figures 2(G,H), figure S8) by 8%.

Segmental resistances during initial stages of programming (before P1, for the device data shown in figure 3(A-C))

Figure S10 shows the initial stages of the programming curve of the device shown in figure 3A, and a table that reports the segmental resistances during the initial stages of programming (figure 3A, figure S10). We see that the segmental resistance of the 'inactive' segment (segment II in figure 3A) just increases by a very small amount (virgin state (210 Ω) to P4 (240 Ω) to P5 (248 Ω)). It saturates at P5 (figure S10). This increase could be a result of dislocation accumulation phenomenon happening near the middle electrode on segment I, just affecting segment II. It should be mentioned here that, in many of the other devices, the 'inactive' segment shows little or no increase in resistance at all during programming.

Local change in TCR. Modeling the disordered region and rest of the wire as resistors in series

In figure S11, we demonstrate another multiple electrode device, which shows that electronic changes occur at a local region on the nanowire. Programming was done between extreme electrodes (figure S11) and it was observed that it neither affected the segmental resistance nor the TCR of the segment between electrodes 1 and 2 (figure S2A). The resistance of the segment between electrodes 2 and 3 contributed to the total increase in resistance. Also, a change in the sign of TCR in this segment was observed, demonstrating that electronic changes contributing to a slope change occur in a local region. It is important to note here that TCR between electrode 1 and 3 (extreme electrodes) did not change its slope, but it did decrease from $0.99\,\Omega/K$ to $0.6\,\Omega/K$ (shown in Figure 3B). Locality proves that devices after programming to a certain stage have metal (positive TCR)+insulator-like disordered (negative TCR) structure in series. The total TCR (it is addition of individual TCR data points just because resistances are additive) can be negative only if the TCR of insulator-like disordered region dominates over that of the metal. This underlines the fact that we do not necessarily have to observe a change in

slope of TCR in all the devices, globally. As shown in Figure 4 in the manuscript, the spatial extent of this disordered region is ~200 nm. Hence it is more likely that we can see a global change in the sign of TCR if the device is shorter owing to a larger relative contribution from the disordered region- as is the case with the device in figure 1A (only ~1 μm long), than if the device is longer- as is the case with segment I of the device shown in figure 3A (~2 μm long). This concept is clearly seen in the data on programmed device shown in figure 1A, which is zoomed into the relevant resistance range and reproduced in figure S12 where we can indeed see the same trends of electron localization observed from figure 5A in the uncorrected (without subtraction) data itself, owing to the short length of the device and a small relative contribution of the background metallic resistance in the total device resistance.

More specifically as far as segment 1 in the device shown in figure 3A is concerned, we estimated the corrected resistance at P2 of the disordered region (figure 5A) by subtracting the virgin phase temperature-resistance data from the global resistance-temperature data at P2 of this segment. Since the exact length of the disordered region for this device is not known, we did not normalize the virgin wire resistance with the length of the wire that remains metallic at P2. However, since the local disordered region is ~ 200 nm (from figure 4) is only ~10% of the actual device length, this missing information does not at all affect the qualitative trends shown in figure 5A.

Data from measurements on 25 GeTe nanowire devices with good ohmic contacts:

We performed temperature-dependent resistance measurements on 25 different devices. Programming curves of all the devices exhibited three regimes, a gradual increase of resistance with voltage, a more rapid increase of resistance with voltage at higher voltages, and finally a discontinuous increase in resistance (either to an amorphous phase or an insulating phase depending upon how controlled the pulses are). Another representative programming curve is shown in figure S13A, with all the regimes indicated.

All the virgin state devices were metallic as shown in the devices in figure 1 and 3. We show virgin state data from two more devices in figure S3, both of which show similar trends as those of a device discussed in figure 1A, i.e. saturation of resistance at low temperatures (<50 K) whereas a linear increase of resistance with temperature at higher temperatures (>50 K).

Upon programming, all the devices initially showed a transition from a virgin metallic state to a disordered-weakly localized state, with disorder-induced effects occurring only in a segment of the wire (in all the multi-electrode devices). Representative data from devices in the weak localization state are shown in figure 1A, figure 3B, figure S11, and figure S14.

Owing to the unstable nature of the insulating single-crystalline phase, controlled programming was required to achieve this phase. We could successfully, by applying just enough amount of disorder via controlled voltage pulsing, convert about 70% of our devices (18 total) to the insulating phase (as represented by a discontinuous change in resistance by half-to-one order of magnitude in the programming curve), and measure VRH conduction characteristics on six of them before they transitioned to the metallic state spontaneously.

Figures 3B in the manuscript shows a representative device, which was converted to an insulating phase (whose characteristics were analyzed in figure 5B). Figure S13B shows VRH characteristics from a second device programmed to an insulating state. Figure S14 shows representative data from a third device, which was progressively converted from a metal to a dirty metal to an insulating phase (showing the same trends as the device in figure 3B of the manuscript).

For structural data we show four different devices (device in figure 1 (movie S1) on which BFTEM imaging was performed, device in figure 2 (movie S3) on which diffraction was performed, and device in figure 4 (DFTEM), and the device in figure S5 (BFTEM showing confirmation of dislocations)), all of which show dislocation/APB migration. Thus with this amount of statistical database collected, it can be concluded that the disorder-induced localization mechanism demonstrated in figure 5C is very general in single-crystalline GeTe nanowires.

APBs or Microtwins?

Another possible reason for the fringes observed in BFTEM images in figure 1, as well as in DFTEM images in figure 4 of the manuscript could be the formation of microtwins. In the event of microtwinning, diffraction suggests (from the direction of spot splitting) that the twin planes are {1-10} planes[17], which are already high symmetry mirror planes in a structure with R3m space group. Hence, twinning– which creates mirror planes that apriori do not exist in a crystal –along {1-10} planes can be ruled out for crystallographic reasons. Also, spot splitting in electron diffraction data progressively moving inwards towards lower order reflections, overwhelmingly shows that these fringes are a result of APBs accumulating (or translational 2D defects; see below for the proof).

Proof that spot splitting in electron diffraction data, Δg is linearly dependent on g (or) presence of disorder in the form of APBs is more easily resolvable in higher order reflections, than in lower order reflections

Spot splitting progressively moving from higher order reflections towards the first order of reflections with increasing disorder clearly deserves more attention. In GeTe, APBs are formed in the {111} family of planes. The observed zone (Zone Axis: [111]) does not consist of {111} planes. The strength of spot splitting (Δg) should hence correspond to the wrong bonds formed by the intersection of these APBs with planes corresponding to the spot g [17]. In other words, intensity of $g \pm \Delta g$ (split spot) increases with the extent of wrong bonds, and intensity of g (original spot) itself relatively decreases. Also Δg is linearly dependent on g. Proof of this fact is as follows: APB is a 2D defect that breaks the translation symmetry of the crystal [17]. As a result, APB creates a phase difference $\phi = g.\Delta r$ in the structure factor S_G, [37,38] where Δr is the displacement amount by which an APB translates the crystal, and g represents the reciprocal space vector (corresponds to planes in real space). In the Fourier space we see this electronic phase difference as $\phi = \Delta g.r$, where the magnitude of spot splitting $|\Delta g| = \frac{g.\Delta r}{|r|\cos\theta}$, θ being

the angle between the fault plane and the planes represented by reciprocal vector g. Hence higher indexed spots (more $|g|$) show more splitting (more $|\Delta g|$).

So the split spot is more resolvable in higher order reflections at low disorder, than in the lower order reflections. As the number of APBs in the {111} planes increases, the extent of wrong bonds in the planes corresponding to g increases. The chance of resolving the split spot in lower indexed planes becomes higher as its intensity increases (at the cost of the original spot). Intersection of two sets of APBs leads to spots splitting in two different directions (figure 4D, still in the higher order reflections). Finally, the split in the first order of reflections in figure 4F (P5) demonstrates an accumulation of huge density of intersecting APBs in {111} planes that has defected the observed {220} plane completely, indicating presence of large density of disordered Te- antisites.

Ordered Te antisites vs. disordered Te antisites:

APBs are formed through condensation of Ge vacancy clusters upon the application of electrical pulses or heat shocks, a process which is theoretically well explained in *ref.7*. Atomistically, condensation of Ge vacancy clusters (which is microstructurally, the formation of APBs) is equivalent to the creation of Te-Te bonds, or ordered Te antisites (see movie S2 for illustration). This ordering of antisites is responsible for the coherent electron scattering effects (*ref 17*) that we show in the DFTEM images in figure 4, and BFTEM images in figure 1. During programming, as we show in the data in figure 4, when more than three sets of APBs causing translational disorder in several <110> directions intersect, they 'lose' their order (as evidenced by the fact that they don't coherently scatter the electron beam resulting in smeared contrast (*ref 17*) in DFTEM image, (see figure 4D). This corresponds on the programming curve to a rapid increase in the resistance (as against a gradual increase), necessitating controlled programming-so as to avoid amorphization. Hence ordered antisites (APBs microstructurally) vs. disordered antisites (series of more than two intersecting APBs microstructurally) is an important distinction in the nature of disorder.

Complementary information given by Fourier space imaging and real space imaging:

Real space imaging and Fourier space imaging together conclusively revealed the presence of dislocations and APBs and their migration. Real space imaging (BFTEM and DFTEM) imaging alone shows a fringe contrast, which when not seen together with the diffraction does not conclusively rule out the possibility of microtwinning for APBs. Also, it is difficult to make qualitative comparisions about the density of APBs in different disordered states, just by performing real-space imaging. Diffraction (as explained in the earlier sections), by virtue of split-spots approaching inwards with more programming clearly shows increasing APB density, as well as rules out the possibility of microtwinning. On the other hand, it is difficult to eliminate the dynamical diffraction effects that arise in diffraction patterns and conclusively establish the presence of APBs and dislocations by just performing diffraction. BFTEM and DFTEM clearly establish this fact. Hence the complementary nature of information given by Fourier space imaging and real space imaging proves the role of APBs (Te antisites) in metal-insulator transition in crystalline GeTe prior to amorphization.

Supplementary figures

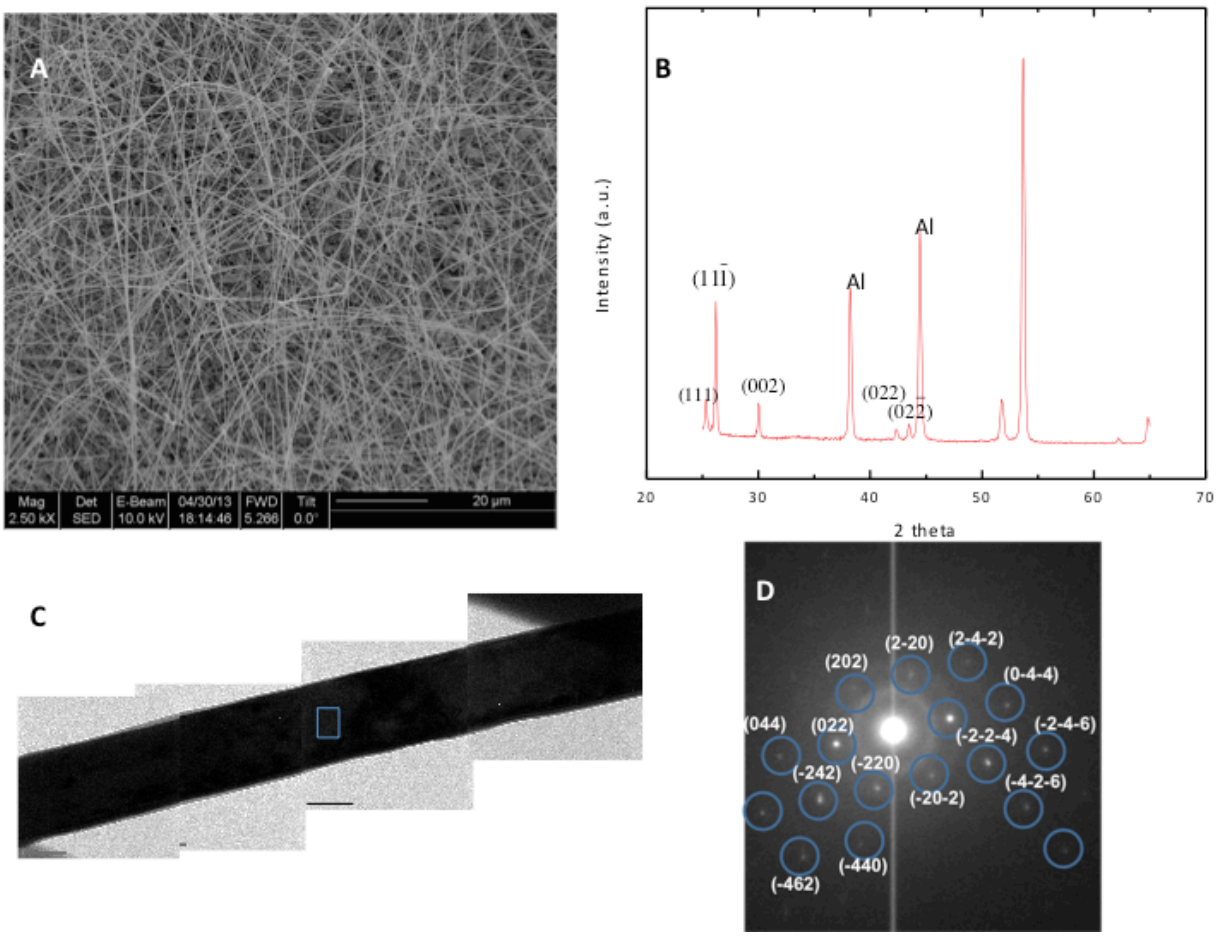

Figure S1: (A) SEM image of the as grown nanowires on a silicon substrate. (B) XRD characterization of the wires from (A) Rhombohedral distortion is evident from splitting up of the (111) peak as (111) and $(11\bar{1})$, and (022) as (022) and $(02\bar{2})$. (C) TEM image of a single nanowire device, data on which is reported in figure 1 of the manuscript. This image was obtained by stitching bright field images in different regions of the nanowire. Scale bar is 100 nm (D) Virgin state selected area electron diffraction pattern from the region bounded by blue lines in (C). The pattern has been indexed in an FCC nomenclature, with $(11\bar{1})$ as the zone axis. The as grown nanowires are relatively defect free.

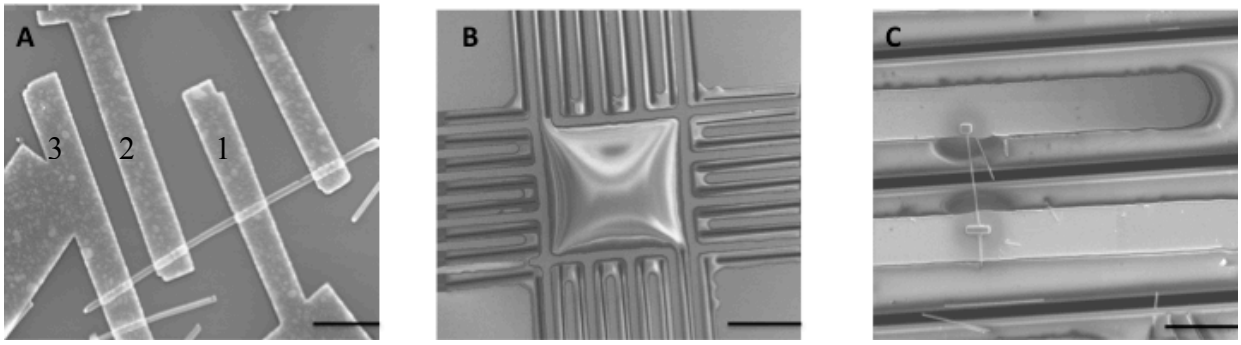

Figure S2: (A) SEM image of a multi-terminal device fabricated via e-beam lithography (see text for details on fabrication). Electrode numbers are indicated. Programming was performed between electrodes 1 and 3 (positive bias was applied to electrode 1 while 3 was grounded). Programming curve and TCR characteristics of this device are discussed in figure S11. Scale bar, $2\,\mu m$. (B) SEM image of a SiNx membrane with fabricated trenches on which TEM compatible devices were assembled. Electrodes were patterned on the membrane platform using photolithography and trenches were made using focused ion beam technique (FIB). Scale bar, $100\ \mu m$. (C) One such device whose structural characteristics are discussed in figure 4 and the associated discussion in the manuscript. Nanowire was clamped to the electrode through platinum deposited using focused ion beam. A thin layer of SiOx (15 nm)[16] was deposited conformally using ALD, following an annealing step at 250^0 C for 20 minutes for better contact properties. Scale bar, $10\,\mu m$.

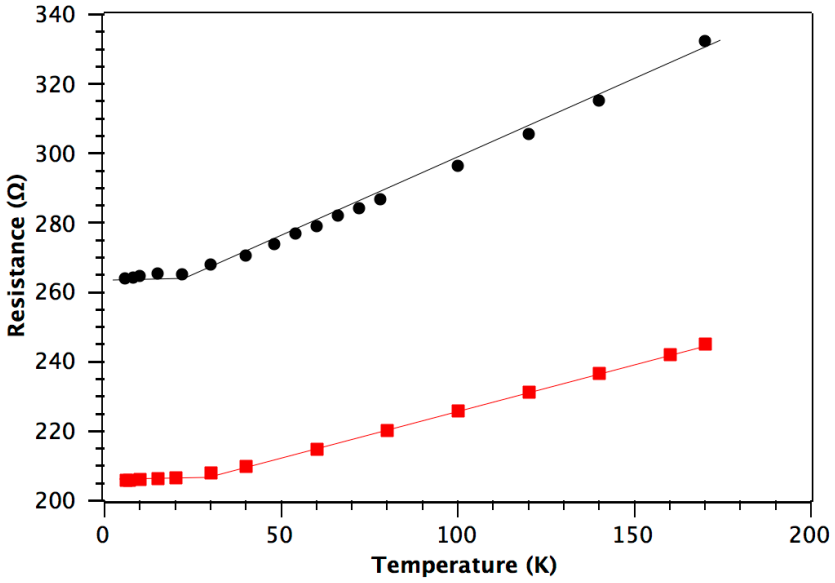

Figure S3: Temperature-dependent resistance data on two more (red and black respectively) GeTe nanowire devices in their virgin state in addition to the device shown in figure 1 of the manuscript. Both of them show a linearly increasing resistance with temperature above 50 K, and approach a saturation value of resistance below 50 K, consistent with metallic behavior described in the manuscript.

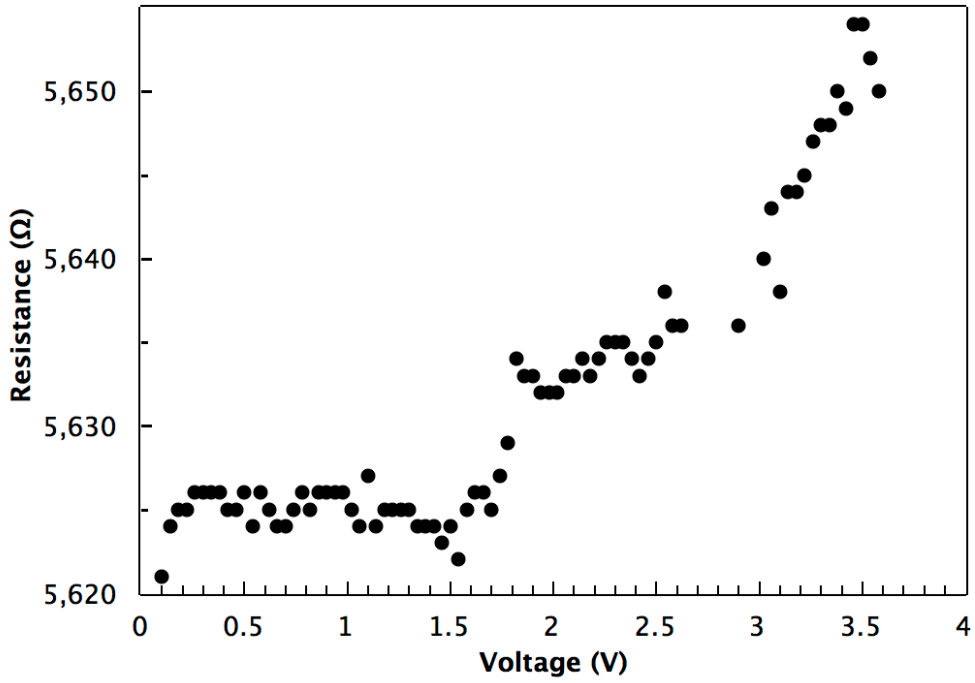

Figure S4: Programming curve for the device shown in movie S1 (snapshots provided in figure 1C-G). Pulse width is 50 ns, and voltage pulses are applied after every 2 seconds. Dislocation and APB formation occurs beyond 0.9 V.

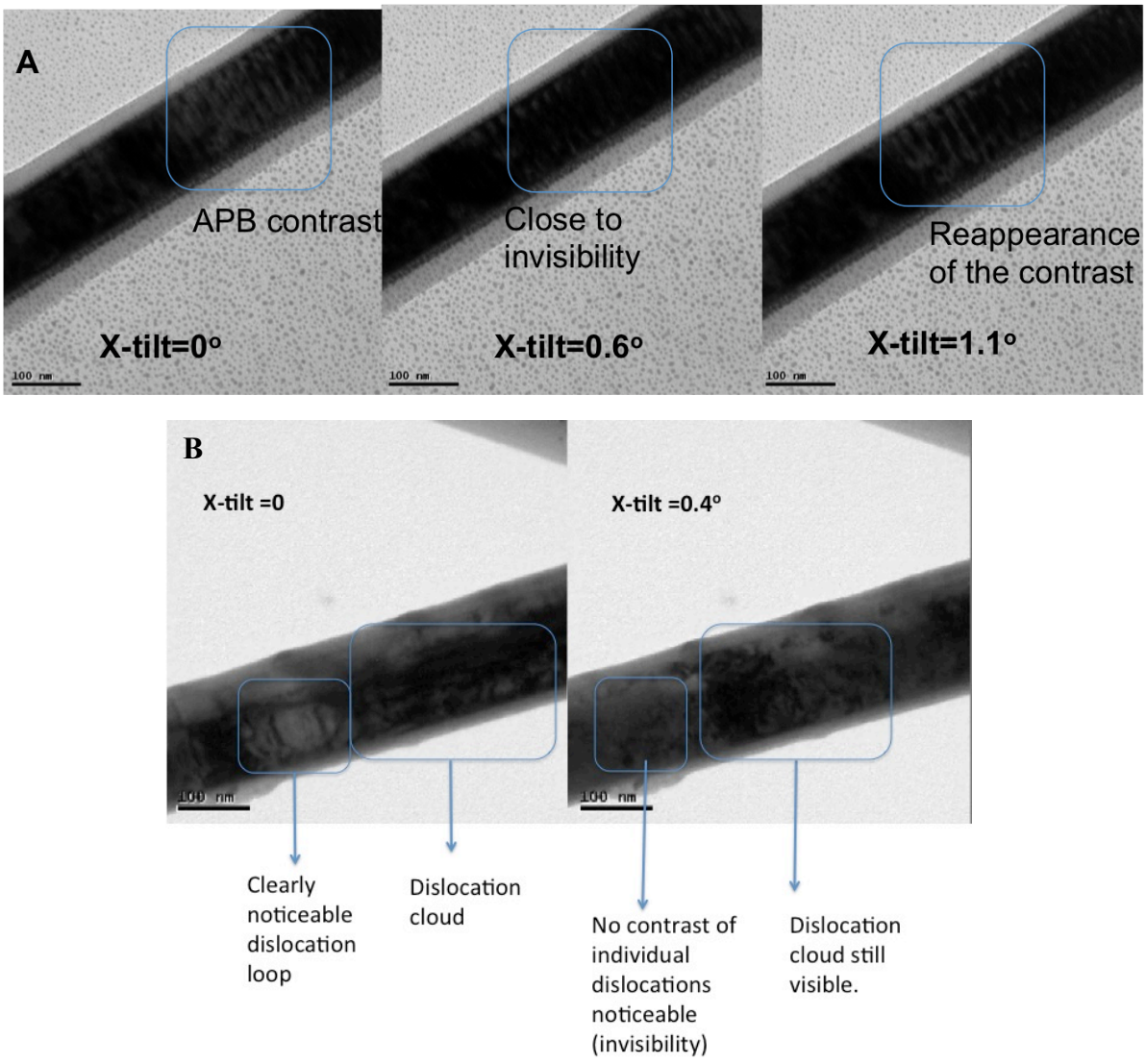

Figure S5: Tilt analysis showing invisibility of dislocations. (A) shows different tilting conditions on the programmed nanowire device shown in movie S1 (snapshots are shown in figures 1C-G in the manuscript), showing invisibility of the dislocation contrast at x-tilt of 0.6°, and its reappearance upon further tilting to 1.1°. (B) shows structural data from a second GeTe nanowire device, showing clear dislocation loops when the nanowire is at zero x-tilt. These loops become invisible with slight x-tilt (of 0.4°). However, upon tilting the dislocation cloud (entangled dislocations) does not become invisible, as although g.b=0, g.(bxu) is non zero [17] in the region where dislocation cloud exists owing to a heavy distortion of the lattice.

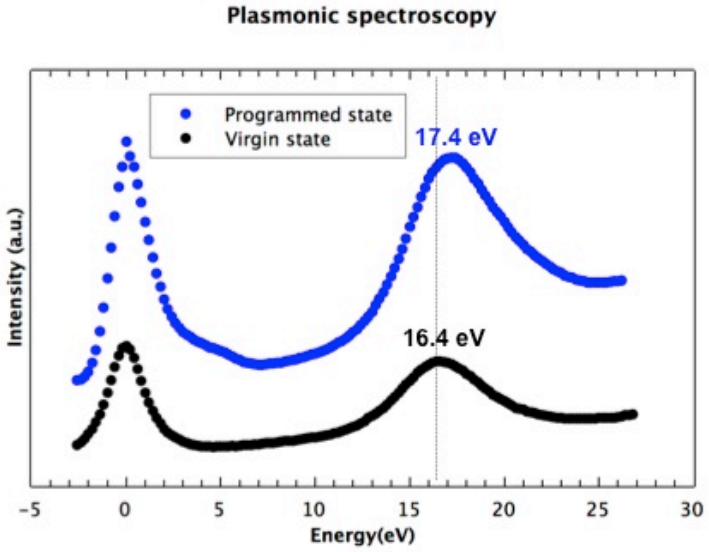

Figure S6: Bulk plasmon peak for GeTe in the virgin state and in programmed state was determined through electron energy loss spectroscopy (EELS). Virgin state shows the bulk plasmon peak at 16.4 eV, whereas after programming (intermediate state), the peak shifts to 17.4 eV. This shift relates to reduction in the hole-carrier concentration. Since in GeTe, Ge vacancies are responsible for hole-generation, removal of holes from the system can be extrapolated as being an effect of condensation of Ge vacancies in the form of vacancy loops or dislocations.

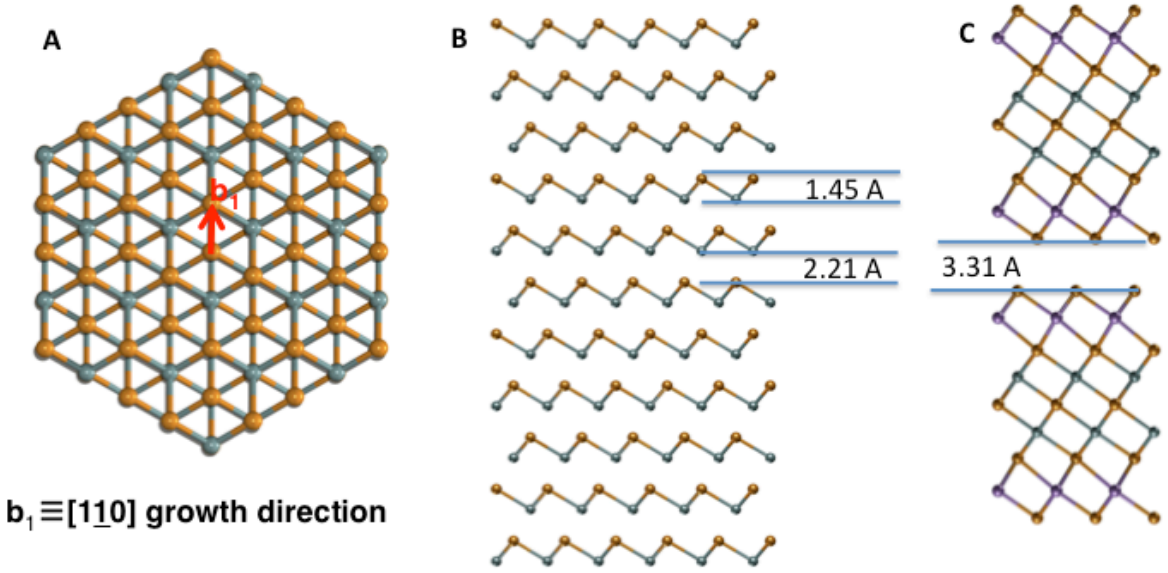

Figure S7: (A) and (B) show GeTe structure relaxed through DFT calculations while (C) shows layered GST ($Ge_2Sb_2Te_5$) structure also relaxed through DFT calculations[4]. (A) shows the (111) (basal plane) of GeTe. Long bonds and short bonds are not apparent. (B) shows the layered structure of GeTe along which the long bonds and short bonds (Peierls distortion) is apparent. Both the long and short bonds are covalent in nature. In both (A) and (B) golden atoms represent Te, blue represent Ge. (C) For comparison, in the layered GST structure, there is van der Waals bonding between the two Te layers (golden atoms) that end and begin a unit cell. An ordered layer of Ge vacancies may be construed as separating these two Te layers. Blue atoms represent Ge, and magenta represents Sb.

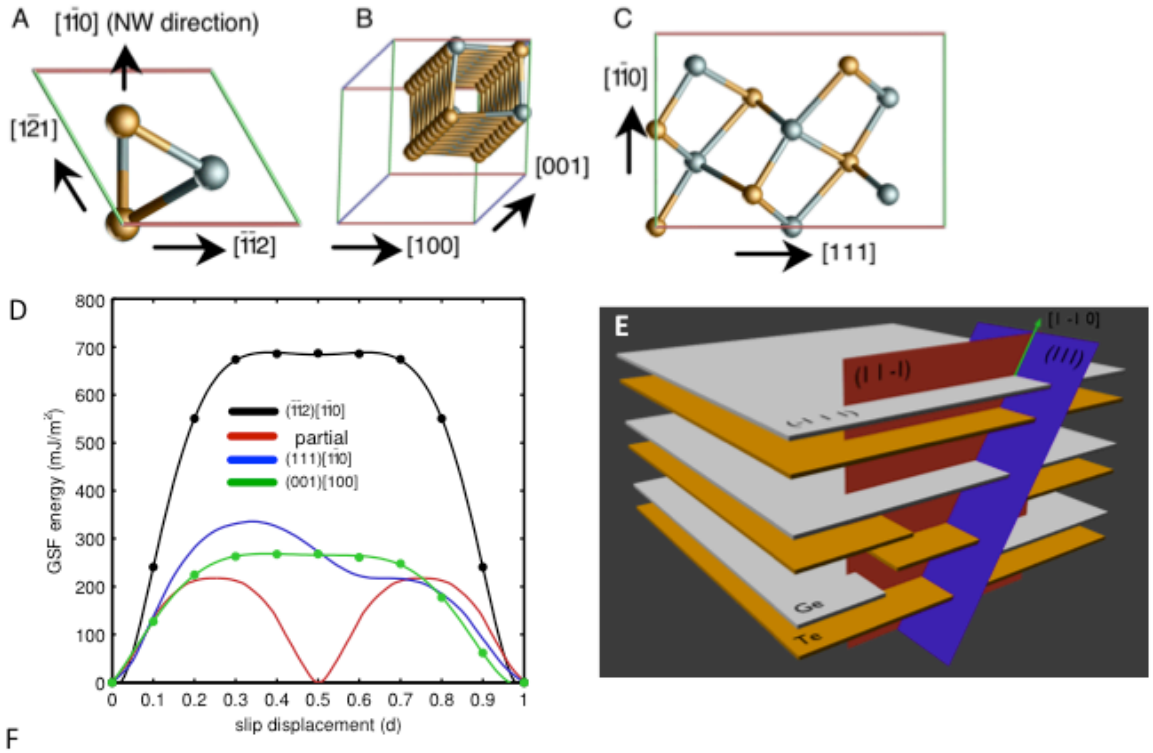

Slip character	GSF energy (mJ/m^2)
(111)[1 -1 0] (direct)	337.6
(111)[1 -1 0] (partial)	217.5
(001)[100]	268.6
(-1 -1 2)[1 -1 0]	686.9

Figure S8: Schematic illustration of (A) slip on basal plane (111) , (B) (001) [100] slip, and (C) ($\bar{1}\bar{1}$2) [1$\bar{1}$0] slip in GeTe. (D) shows the results of DFT calculations of generalized-stacking-fault (GSF) energy for three different slip-characters. Table in (F) shows a comparison of maximum GSF on different slip systems. As commented in the text, presence of Ge vacancies contributes to the decrease of these values. (E) shows the dynamics of dislocation formed in ($\bar{1}$11) plane, with segments in (111) and (11$\bar{1}$) planes and gliding along [1$\bar{1}$0] (growth direction). This case, as an example, was discussed in the text. The dislocation glide in {111} planes can easily happen through the formation of partials, as shown by the table in (F).

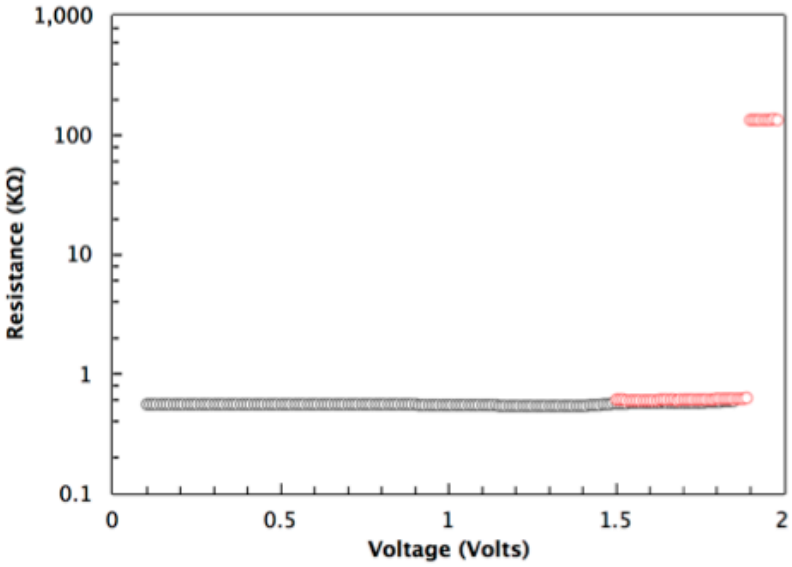

Figure S9: Programming curve of a device that was amorphized (>500 fold increase in resistance at 1.9 V applied voltage pulse). Controlled programming was not performed on this device and hence it amorphized, indicating the role of electronic instabilities in amorphization.

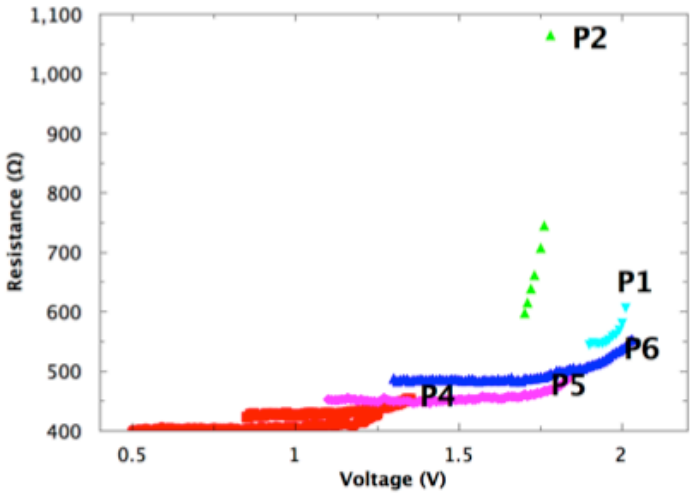

Position on the programming curve shown above	Resistance of segment I in figure 2A	Resistance of segment II in figure 2A
P4	257 Ω	239 Ω
P5	290 Ω	248 Ω
P6	350 Ω	248 Ω

Figure S10: Complete programming curve up to P2 of the device shown in figure 3A in the manuscript. The table elucidates that increase in resistance of the entire nanowire comes from local region in segment I. Apart from a small initial increase in resistance; segment II does not show any appreciable change upon programming.

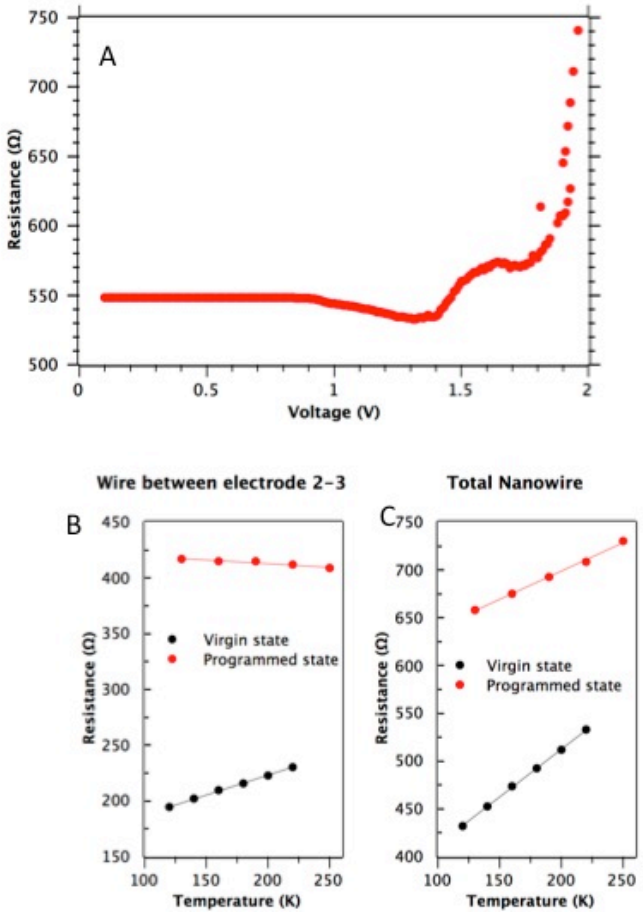

Figure S11: (A) Programming curve of another three terminal device. (B) T-R characteristics of the segment between electrodes 2 and 3 that shows the effect of disorder. In this device, we can clearly observe change of sign for TCR. (C) T-R characteristics of the total nanowire. TCR reduces from $0.99\,{}^{\Omega}\!/_{K}$ to $0.6\,{}^{\Omega}\!/_{K}$, but does not become negative for the entire nanowire This indicates that since the effect of disorder is local, a global change in the sign of TCR need not be observed for the entire device.

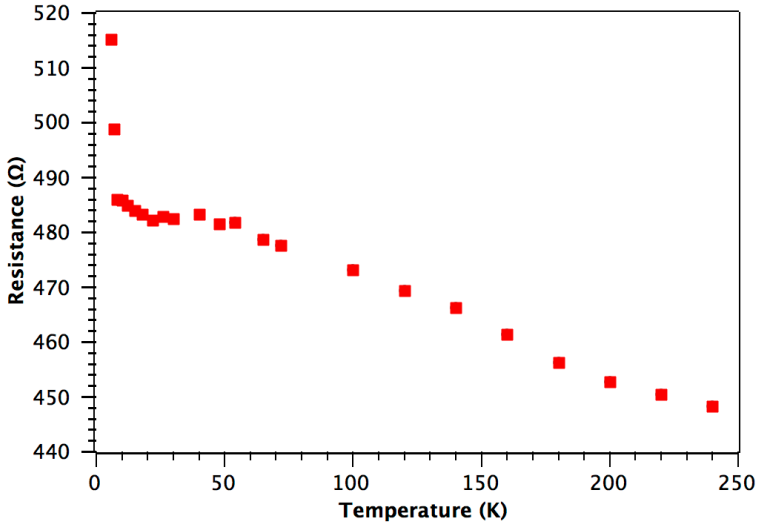

Figure S12: Zoomed-in temperature-resistance data of the programmed GeTe nanowire device in the disordered phase (same as figure 1 A (red squares)). The data (*uncorrected*) is from a short device where the relative contribution from the background metallic state is expected to be small and hence shows the same trends as in Figure 5A.

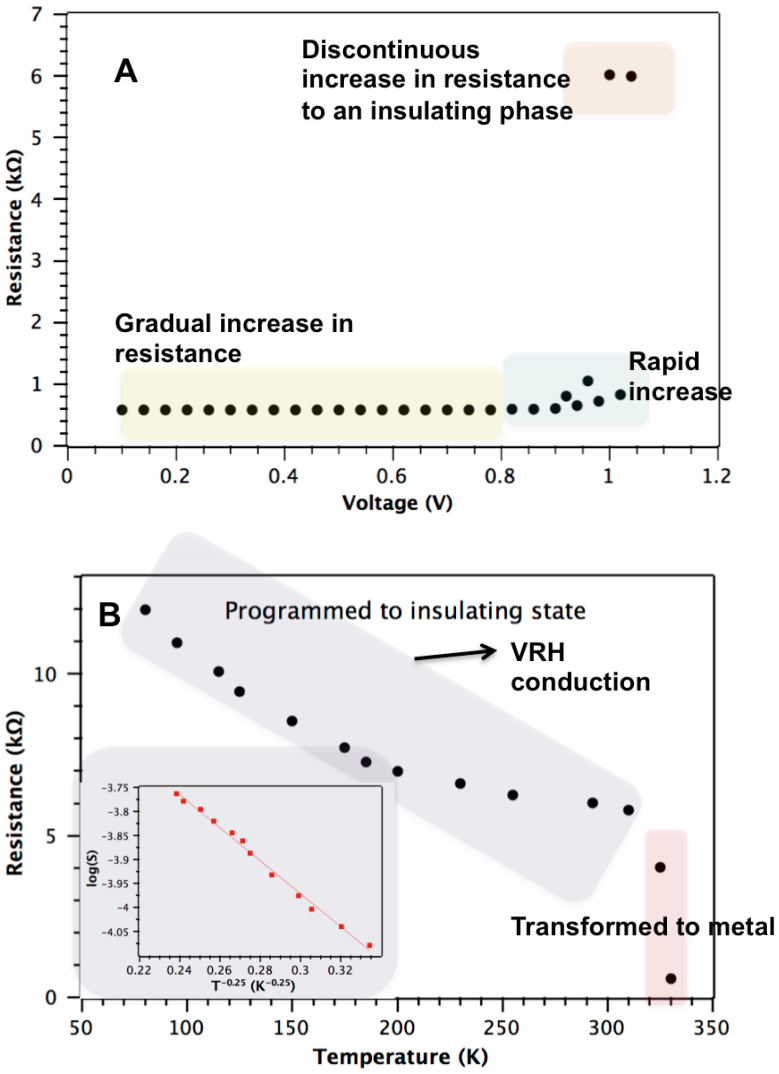

Figure S13: Characterization of the insulating state upon programming. (A) Programming curve for a GeTe nanowire device programmed to an insulating state. Notice the key features in the programming curve, i.e. a gradual increase in the resistance to a rapid increase to a sudden discontinuous increase by an order of magnitude. This is an insulating phase as characterized in (B). (B) Temperature-dependent resistance measurements of the device programmed to insulating state (programming curve is shown in A). Notice the VRH conduction (inset) up to 320 K, and then a transformation to metallic phase much like the device shown in figure 5B of the manuscript.

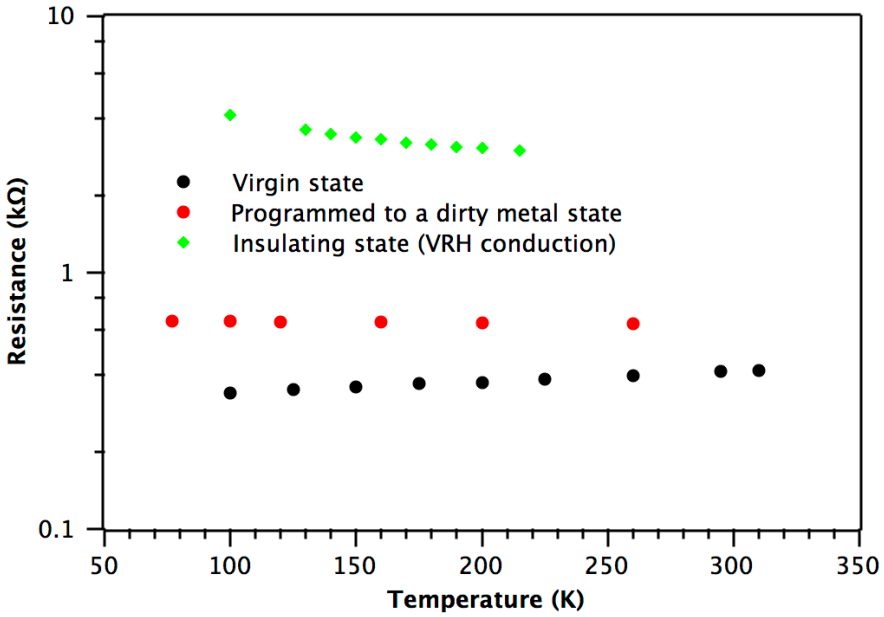

Figure S14: Temperature-resistance data on another device showing progression from virgin state to a dirty-metal state to an insulating state, which shows VRH conduction.

References:

4. Nam, S.-W., et al. Electrical wind force–driven and dislocation-templated amorphization in phase-change nanowires, *Science* **336**, 1561 (2012).

5. Edwards,A.H., et al. Electronic structure of intrinsic defects in crystalline germanium telluride, *Phys. Rev. B* **73**, 045210 (2006).

6. Edwards,A.H., Pineda,A.C., Schultz, P.A., Martin, M.G., Thompson, A.P., Hjalmarson, H.P., Theory of persistent, p-type, metallic conduction in c-GeTe, *J. Phys: Condens. Matter.* **17**, L329 (2005).

7. Deringer, M. L. V.L., Stoffel, R.P., Dronskowski, R., Mechanisms of atomic motion through crystalline GeTe, *Chem.Mater.,* **25**, 2220 (2013).

15. Raether, H., *Excitation of plasmons and interband transitions by electrons,* (springer tracts in modern physics, vol. 88).

16. Meister, S., Schoen, D. T., Topinka, M. A., Minor, A. M., Cui, Y., Void Formation Induced Electrical Switching in Phase-Change Nanowires, *Nanolett.* **8**, 4562 (2008).

17. Carter, C.B., Williams, D. B., Transmission electron microscopy: a textbook for materials science. (Springer, New York, 1996).

36. Rotunno, E., Lazzarini, L., Longo, M., Grillo, V., Crystal structure assessment of Ge–Sb–Te phase change nanowires *Nanoscale* **5**, 1557, (2013).

37. Kittel, C., Introduction to solid state physics, (8^{th} edition, Wiley & Sons, New York, 2005)

38. Fultz, B and Howe, J, Transmission electron microscopy and diffractometry of materials, (4^{th} edition, Springer, New York, 2008)

Supplementary movie captions:

Movie S1: BFTEM movie of a GeTe nanowire device showing the migration of APB contrast and dislocations along the hole-wind force direction, during the initial stages of programming. Voltage pulses were applied with increments of from 0.1 V after every two seconds. The movie begins at ~0.7 V when the APBs are just about to be formed and is played at 2X speed.

Movie S2: Illustration of dislocation dynamics also represented in figure S8 (E). This movie shows creation of a dislocation through vacancy condensation, which creates an anti-phase boundary (APB), its motion in the region of interest; and passage of a subsequent dislocation (generated elsewhere), which cleans up the APB created by the first dislocation.

Movie S3: Shows the evolution of diffraction pattern from a local region of wire shown in figure S1 and discussed in figures 2C-G as a function of programming (programming curve is shown in figure 2A). The movie is played at 3X speed. Voltage pulses are applied after every two seconds, and the movie starts when the applied voltage pulse is at 1.12 V (during programming). We can see spots splitting and healing, forbidden spots coming up and healing subsequently. Nothing much happens to the diffraction spots below 1.12 V pulses.